WAVE MOTION 10 (1988) 547-582
NORTH-HOLLAND

REVIEW OF THE FORMULATION AND APPLICATIONS OF THE FINITE-DIFFERENCE TIME-DOMAIN METHOD FOR NUMERICAL MODELING OF ELECTROMAGNETIC WAVE INTERACTIONS WITH ARBITRARY STRUCTURES

Allen TAFLOVE

Department of Electrical Engineering and Computer Science, Technological Institute, Northwestern University, Evanston, IL 60201, U.S.A.

Received 1 April 1988, Revised 15 May 1988

This paper reviews the basis and applications of the finite-difference time-domain (FD-TD) numerical modeling approach for Maxwell's equations. FD-TD is very simple in concept and execution. However, it is remarkably robust, providing highly accurate modeling predictions for a wide variety of electromagnetic wave interaction problems. The accuracy and breadth of FD-TD applications will be illustrated by a number of two- and three-dimensional examples. The objects modeled range in nature from simple geometric shapes to extremely complex aerospace and biological systems. In all cases where rigorous analytical, code-to-code, or experimental validations are possible, FD-TD predictive data for penetrating and scattered near fields as well as radar cross sections are in excellent agreement with the benchmarks. It will also be shown that opportunities are arising in applying FD-TD to model rapidly time-varying systems, microwave circuits, and inverse scattering. With continuing advances in FD-TD modeling theory as well as continuing advances in supercomputer technology, there is a strong possibility that FD-TD numerical modeling will occupy an important place in high-frequency engineering electromagnetics as we move into the 1990s.

1. Introduction

Accurate numerical modeling of full-vector electromagnetic wave interactions with arbitrary structures is difficult. Typical structures of engineering interest have shapes, apertures, cavities, and material compositions or surface loadings which produce near fields that cannot be resolved into finite sets of modes or rays. Proper numerical modeling of such near fields requires sampling at sub-wavelength resolution to avoid aliasing of magnitude and phase information. The goal is to provide a self-consistent model of the mutual coupling of the electrically-small cells comprising the structure.

This paper reviews the formulation and applications of a candidate numerical modeling approach for this purpose: the finite-difference time-domain (FD-TD) solution of Maxwell's curl equations. FD-TD is analogous to existing finite-difference solutions of scalar wave propagation and fluid-flow problems in that the numerical model is based upon a direct solution of the governing partial differential equation. Yet, FD-TD is a nontraditional approach to numerical electromagnetic wave modeling of complex structures for engineering applications, where frequency-domain integral equation approaches such as the method of moments have dominated for 25 years (see the article by Umashankar in this issue).

One of the goals of this paper is to demonstrate that recent advances in FD-TD modeling concepts and software implementation, combined with advances in computer technology, have expanded the scope, accuracy, and speed of FD-TD modeling to the point where it may be the preferred choice for certain types of electromagnetic wave penetration, scattering, guiding, and inverse scattering

problems. With this in mind, this paper will succinctly review the following FD-TD modeling validations and examples:

(1) electromagnetic wave scattering, two dimensions:
  (a) square metal cylinder, TM polarization,
  (b) circular muscle-fat layered cylinder, TE polarization,
  (c) homogeneous, anisotropic, square material cylinder, TM polarization,
  (d) circular metal cylinder, conformally modeled, TE and TM polarization,
  (e) flanged metal open cavity,
  (f) relativistically vibrating mirror, oblique incidence;
(2) electromagnetic wave scattering, three dimensions:
  (a) metal cube, broadside incidence,
  (b) flat conducting plate, multiple monostatic looks,
  (c) T-shaped conducting target, multiple monostatic looks;
(3) electromagnetic wave penetration and coupling, two and three dimensions:
  (a) narrow slots and lapped joints in thick screens,
  (b) wires and wire bundles in free space and in a metal cavity;
(4) very complex three-dimensional structures:
  (a) missile seeker section,
  (b) inhomogeneous tissue model of the entire human body;
(5) microstrip and microwave circuit models,
(6) inverse scattering reconstructions in one and two dimensions.

Finally, this paper will conclude with a discussion of computing resources for FD-TD and the potential impact of massively concurrent machines.

2. General characteristics of FD-TD

As stated, FD-TD is a direct solution of Maxwell's time-dependent curl equations. It employs no potential. Instead, it applies simple, second-order accurate central-difference approximations [1] for the space and time derivatives of the electric and magnetic fields directly to the respective differential operators of the curl equations. This achieves a sampled-data reduction of the continuous electromagnetic field in a volume of space, over a period of time. Space and time discretizations are selected to bound errors in the sampling process, and to ensure numerical stability of the algorithm [2]. Electric and magnetic field components are interleaved in space to permit a natural satisfaction of tangential field continuity conditions at media interfaces. Overall, FD-TD is a marching-in-time procedure which simulates the continuous actual waves by sampled-data numerical analogs propagating in a data space stored in a computer. At each time step, the system of equations to update the field components is fully explicit, so that there is no need to set up or solve a set of linear equations, and the required computer storage and running time is proportional to the electrical size of the volume modeled.

Figure 1(a) illustrates the time-domain wave tracking concept of the FD-TD method. A region of space within the dashed lines is selected for field sampling in space and time. At time =0, it is assumed that all fields within the numerical sampling region are identically zero. An incident plane wave is assumed to enter the sampling region at this point. Propagation of the incident wave is modeled by the commencement of time-stepping, which is simply the implementation of the finite-difference analog of the curl equations. Time-stepping continues as the numerical analog of the incident wave strikes the modeled target embedded within the sampling region. All outgoing scattered wave analogs ideally propagate through the lattice truncation planes with negligible reflection to exit the sampling region. Phenomena such as induction of surface currents, scattering and multiple scattering, penetration through apertures, and cavity excitation are modeled time-step by time-step by the action of the curl equations analog. Self-consistency of these modeled phenomena is gen-

Fig. 1. Basic elem
domain wave track

erally assured
ations are wel
sampling proc
Time-steppi
late-time pulse
is observed. A
the sinusoidal
wave is assume
and time-stepp
the sampling r
This is a conse
principle [3].
tion with FD-T
complete cycles
be time-stepped

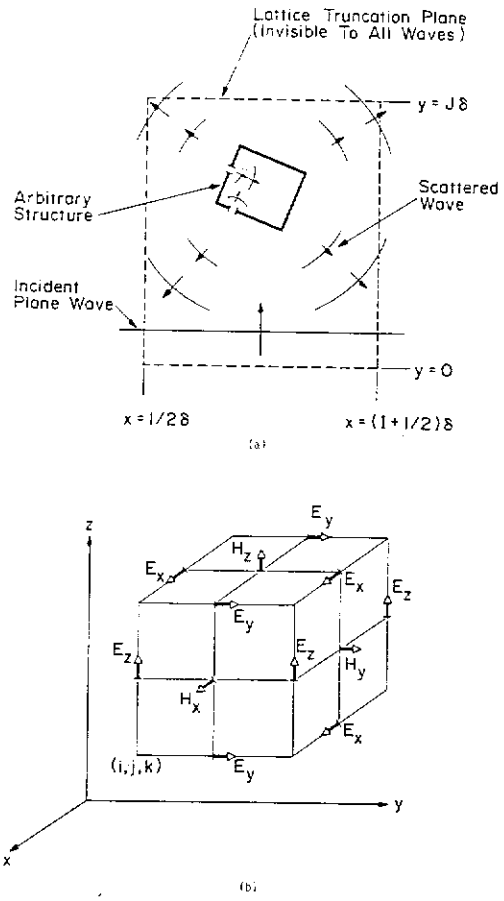

Fig. 1. Basic elements of the FD-TD space lattice: (a) time-domain wave tracking concept; (b) lattice unit cell in Cartesian coordinates.

erally assured if their spatial and temporal variations are well resolved by the space and time sampling process.

Time-stepping is continued until the desired late-time pulse response or steady-state behavior is observed. An important example of the latter is the sinusoidal steady state, wherein the incident wave is assumed to have a sinusoidal dependence, and time-stepping is continued until all fields in the sampling region exhibit sinusoidal repetition. This is a consequence of the limiting amplitude principle [3]. Extensive numerical experimentation with FD-TD has shown that the number of complete cycles of the incident wave required to be time-stepped to achieve the sinusoidal steady state is approximately equal to the Q-factor of the structure or phenomenon being modeled.

Figure 1(b) illustrates the positions of the electric and magnetic field components about a unit cell of the FD-TD lattice in Cartesian coordinates [1]. Note that each magnetic field vector component is surrounded by four circulating electric field vector components, and vice versa. This arrangement permits not only a centered-difference analog to the space derivatives of the curl equations, but also a natural geometry for implementing the integral form of Faraday's Law and Ampere's Law at the space-cell level. This integral interpretation permits a simple but effective modeling of the physics of thin-slot coupling, thin-wire coupling, and smoothly curved target surfaces, as will be seen later.

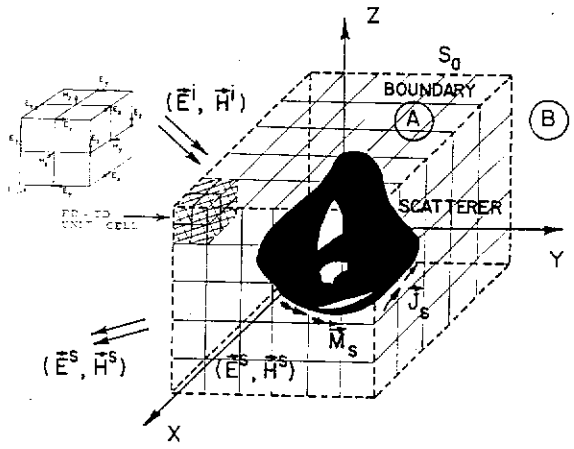

Fig. 2. Arbitrary three-dimensional scatterer embedded in an FD-TD lattice.

Figure 2 illustrates how an arbitrary three-dimensional scatterer is embedded in an FD-TD space lattice comprised of the unit cells of Fig. 1(b). Simply, the desired values of electrical permittivity and conductivity are assigned to each electric field component of the lattice. Correspondingly, desired values of magnetic permeability and equivalent conductivity are assigned to each magnetic field component of the lattice. The media parameters are interpreted by the FD-TD program as local coefficients for the time-stepping

algorithm. Specification of media properties in this component-by-component manner results in a stepped-edge, or staircase approximation of curved surfaces. Continuity of tangential fields is assured at the interface of dissimilar media with this procedure. There is no need for special field matching at media interface points. Stepped-edge approximation of curved surfaces has been found to be adequate in the FD-TD modeling problems studied in the 1970s and early 1980s, including wave interactions with biological tissues [4], penetration into cavities [5, 6], and electromagnetic pulse (EMP) interactions with complex structures [7–9]. However, recent interest in wide dynamic range models of scattering by curved targets has prompted the development of surface-conforming FD-TD approaches which eliminate stair-casing. These will be summarized later in this paper.

3. Basic FD-TD algorithm details

3.1. Maxwell's equations

Consider a region of space which is source-free and has constitutive electrical parameters that are independent of time. Then, using the MKS system of units, Maxwell's curl equations are given by

$$\frac{\partial \boldsymbol{H}}{\partial t} = -\frac{1}{\mu}\nabla \times \boldsymbol{E} - \frac{\rho'}{\mu}\boldsymbol{H}, \tag{1}$$

$$\frac{\partial \boldsymbol{E}}{\partial t} = \frac{1}{\varepsilon}\nabla \times \boldsymbol{H} - \frac{\sigma}{\varepsilon}\boldsymbol{E} \tag{2}$$

where E is the electric field in volts/meter; H is the magnetic field in amperes/meter; ε is the electrical permittivity in farads/meter; σ is the electrical conductivity in mhos/meter (siemens/meter); μ is the magnetic permeability in henrys/meter; and ρ' is an equivalent magnetic resistivity in ohms/meter. (The magnetic resistivity term is provided to yield symmetric curl equations, and allow for the possibility of a magnetic field loss mechanism.) Assuming that ε, σ, μ, and ρ' are isotropic, the following system of scalar equations is equivalent to Maxwell's curl equations in the rectangular coordinate system (x, y, z):

$$\frac{\partial H_x}{\partial t} = \frac{1}{\mu}\left(\frac{\partial E_y}{\partial z} - \frac{\partial E_z}{\partial y} - \rho' H_x\right), \tag{3a}$$

$$\frac{\partial H_y}{\partial t} = \frac{1}{\mu}\left(\frac{\partial E_z}{\partial x} - \frac{\partial E_x}{\partial z} - \rho' H_y\right), \tag{3b}$$

$$\frac{\partial H_z}{\partial t} = \frac{1}{\mu}\left(\frac{\partial E_x}{\partial y} - \frac{\partial E_y}{\partial x} - \rho' H_z\right); \tag{3c}$$

$$\frac{\partial E_x}{\partial t} = \frac{1}{\varepsilon}\left(\frac{\partial H_z}{\partial y} - \frac{\partial H_y}{\partial z} - \sigma E_x\right), \tag{4a}$$

$$\frac{\partial E_y}{\partial t} = \frac{1}{\varepsilon}\left(\frac{\partial H_x}{\partial z} - \frac{\partial H_z}{\partial x} - \sigma E_y\right), \tag{4b}$$

$$\frac{\partial E_z}{\partial t} = \frac{1}{\varepsilon}\left(\frac{\partial H_y}{\partial x} - \frac{\partial H_x}{\partial y} - \sigma E_z\right). \tag{4c}$$

The system of six coupled partial differential equations of (3) and (4) forms the basis of the FD-TD algorithm for electromagnetic wave interactions with general three-dimensional objects. Before proceeding with the details of the algorithm, it is informative to consider one important simplification of the full three-dimensional case. Namely, if we assume that neither the incident plane wave excitation nor the modeled geometry has any variation in the z-direction (i.e., all partial derivatives with respect to z equal zero), Maxwell's curl equations reduce to two decoupled sets of scalar equations. These decoupled sets, termed the transverse magnetic (TM) mode and the transverse electric (TE) mode, describe two-dimensional wave interactions with objects. The relevant equations for each case follow:

- *TM case* (E_z, H_x, and H_y field components only)

$$\frac{\partial H_x}{\partial t} = -\frac{1}{\mu}\left(\frac{\partial E_z}{\partial y} + \rho' H_x\right), \tag{5a}$$

$$\frac{\partial H_y}{\partial t} = \frac{1}{\mu}\left(\frac{\partial E_z}{\partial x} - \rho' H_y\right), \tag{5b}$$

$$\frac{\partial E_z}{\partial t} = \frac{1}{\varepsilon}\left(\frac{\partial H_y}{\partial x} - \frac{\partial H_x}{\partial y} - \sigma E_z\right); \tag{5c}$$

- TE case (H_z, E_x, and E_y field components only)

$$\frac{\partial E_x}{\partial t}=\frac{1}{\varepsilon}\left(\frac{\partial H_z}{\partial y}-\sigma E_x\right), \tag{6a}$$

$$\frac{\partial E_y}{\partial t}=-\frac{1}{\varepsilon}\left(\frac{\partial H_z}{\partial x}+\sigma E_y\right), \tag{6b}$$

$$\frac{\partial H_z}{\partial t}=\frac{1}{\mu}\left(\frac{\partial E_x}{\partial y}-\frac{\partial E_y}{\partial x}-\rho' H_z\right). \tag{6c}$$

3.2. The Yee algorithm

In 1966, Yee [1] introduced a set of finite-difference equations for the system of (3) and (4). Following Yee's notation, we denote a space point in a rectangular lattice as

$$(i, j, k)=(i\,\Delta x, j\,\Delta y, k\,\Delta z) \tag{7a}$$

and any function of space and time as

$$F^n(i, j, k)=F(i\,\Delta x, j\,\Delta y, k\,\Delta z, n\,\Delta t) \tag{7b}$$

where Δx, Δy, and Δz are, respectively, the lattice space increments in the x-, y-, and z-coordinate directions; Δt is the time increment; and i, j, k, and n are integers. Yee used centered finite-difference expressions for the space and time derivatives that are both simply programmed and second-order accurate in the space and time increments respectively:

$$\frac{\partial F^n(i, j, k)}{\partial x}=\frac{F^n(i+\tfrac{1}{2}, j, k)-F^n(i-\tfrac{1}{2}, j, k)}{\Delta x}+O(\Delta x^2), \tag{8a}$$

$$\frac{\partial F^n(i, j, k)}{\partial t}=\frac{F^{n+1/2}(i, j, k)-F^{n-1/2}(i, j, k)}{\Delta t}+O(\Delta t^2). \tag{8b}$$

To achieve the accuracy of (8a), and to realize all of the required space derivatives of the system of (3) and (4), Yee positioned the components of $\boldsymbol{E}$ and $\boldsymbol{H}$ about a unit cell of the lattice as shown in Fig. 1(**b**). To achieve the accuracy of (8**b**), he evaluated $\boldsymbol{E}$ and $\boldsymbol{H}$ at alternate half time steps. The following are sample finite-difference time-stepping expressions for a magnetic and an electric field component resulting from these assumptions:

$$\begin{aligned}H_x^{n+1/2}(i, j+\tfrac{1}{2}, k+\tfrac{1}{2})&=\frac{1-\dfrac{\rho'(i, j+\frac{1}{2}, k+\frac{1}{2})\Delta t}{2\mu(i, j+\frac{1}{2}, k+\frac{1}{2})}}{1+\dfrac{\rho'(i, j+\frac{1}{2}, k+\frac{1}{2})\Delta t}{2\mu(i, j+\frac{1}{2}, k+\frac{1}{2})}}\cdot H_x^{n-1/2}(i, j+\tfrac{1}{2}, k+\tfrac{1}{2})\\&+\frac{\Delta t}{\mu(i, j+\frac{1}{2}, k+\frac{1}{2})}\cdot\left[1+\frac{\rho'(i, j+\frac{1}{2}, k+\frac{1}{2})\Delta t}{2\mu(i, j+\frac{1}{2}, k+\frac{1}{2})}\right]^{-1}\\&\times\{[E_y^n(i, j+\tfrac{1}{2}, k+1)-E_y^n(i, j+\tfrac{1}{2}, k)]/\Delta z\\&+[E_z^n(i, j, k+\tfrac{1}{2})-E_z^n(i, j+1, k+\tfrac{1}{2})]/\Delta y\},\end{aligned} \tag{9}$$

$$\begin{aligned}E_z^{n+1}(i, j, k+\tfrac{1}{2})&=\frac{1-\dfrac{\sigma(i, j, k+\frac{1}{2})\Delta t}{2\varepsilon(i, j, k+\frac{1}{2})}}{1+\dfrac{\sigma(i, j, k+\frac{1}{2})\Delta t}{2\varepsilon(i, j, k+\frac{1}{2})}}\cdot E_z^n(i, j, k+\tfrac{1}{2})\\&+\frac{\Delta t}{\varepsilon(i, j, k+\frac{1}{2})}\cdot\left[1+\frac{\sigma(i, j, k+\frac{1}{2})\Delta t}{2\varepsilon(i, j, k+\frac{1}{2})}\right]^{-1}\\&\times\{[H_y^{n+1/2}(i+\tfrac{1}{2}, j, k+\tfrac{1}{2})-H_y^{n+1/2}(i-\tfrac{1}{2}, j, k+\tfrac{1}{2})]/\Delta x\\&+[H_x^{n+1/2}(i, j-\tfrac{1}{2}, k+\tfrac{1}{2})-H_x^{n+1/2}(i, j+\tfrac{1}{2}, k+\tfrac{1}{2})]/\Delta y\}.\end{aligned} \tag{10}$$

With the system of finite-difference equations represented by (9) and (10), the new value of a field vector component at any lattice point depends only on its previous value and on the previous values of the components of the other field vector at adjacent points. Therefore, at any given time step, the computation of a field vector can proceed

either one point at a time; or, if p parallel processors are employed concurrently, p points at a time.

3.3. Numerical stability

To ensure the stability of the time-stepping algorithm exemplified by (9) and (10), Δt is chosen to satisfy the inequality [2, 10]

$$c_{\max}\Delta t \leq \left\{\frac{1}{\Delta x^2}+\frac{1}{\Delta y^2}+\frac{1}{\Delta z^2}\right\}^{-1/2} \tag{11}$$

where $c_{\max}$ is the maximum electromagnetic wave phase velocity within the media being modeled. Note that the corresponding numerical stability criterion set forth in (7) and (8) of reference [1] is incorrect (cf. [2]). For the TM and TE two-dimensional modeling cases, it can be shown [10] that the modified time-step limit for numerical stability is obtained from (11) simply by setting $\Delta z = \infty$.

3.4. Numerical dispersion

The numerical algorithm for Maxwell's curl equations represented by (9) and (10) causes dispersion of the simulated wave modes in the computational lattice. That is, the phase velocity of numerical modes in the FD-TD lattice can vary with modal wavelength, direction of propagation, and lattice discretization. This numerical dispersion can lead to nonphysical results such as pulse distortion, artificial anisotropy, and pseudorefraction. Numerical dispersion is a factor in FD-TD modeling that must be accounted to understand the operation of the algorithm and its accuracy limits.

Following the analysis in [10], it can be shown that the numerical dispersion relation for the three-dimensional case represented by (9) and (10) is given by

$$\left(\frac{1}{c\Delta t}\right)^2 \sin^2(\tfrac{1}{2}\omega\Delta t) = \frac{1}{\Delta x^2}\sin^2(\tfrac{1}{2}k_x\Delta x) + \frac{1}{\Delta y^2}\sin^2(\tfrac{1}{2}k_y\Delta y)+\frac{1}{\Delta z^2}\sin^2(\tfrac{1}{2}k_z\Delta z) \tag{12}$$

where k_x, k_y, and k_z are, respectively, the x-, y-, and z-components of the wavevector; ω is the wave angular frequency; and c is the speed of light in the homogeneous material being modeled.

In contrast to the numerical dispersion relation, the analytical dispersion relation for a plane wave in a continuous, lossless medium is just

$$\omega^2/c^2 = k_x^2 + k_y^2 + k_z^2 \tag{13}$$

for the three-dimensional case. Although, at first glance, (12) bears little resemblance to the ideal case of (13), we can easily show that (12) reduces to (13) in the limit as Δt, Δx, Δy, and Δz all go to zero. Qualitatively, this suggests that numerical dispersion can be reduced to any degree that is desired if we only use a fine-enough FD-TD gridding.

To quantitatively illustrate the dependence of numerical dispersion upon FD-TD grid discretization, we shall take as an example the two-dimensional TM case ($\Delta z = \infty$), assuming for simplicity square unit cells ($\Delta x = \Delta y = \Delta$) and wave propagation at an angle α with respect to the positive x-axis ($k_x = k\cos\alpha$; $k_y = k\sin\alpha$). Then, dispersion relation (12) simplifies to

$$\left(\frac{\Delta}{c\Delta t}\right)^2 \sin^2(\tfrac{1}{2}\omega\Delta t) = \sin^2(\tfrac{1}{2}k\cos\alpha\,\Delta)+\sin^2(\tfrac{1}{2}k\sin\alpha\,\Delta). \tag{14}$$

Equation (14) can be conveniently solved for the wavevector magnitude, k, by applying Newton's method. This process is especially convenient if Δ is normalized to the free-space wavelength.

Figure 3(a) provides results using this procedure which illustrate the variation of numerical phase velocity with wave propagation angle in the FD-TD grid. Three different grid resolutions of the propagating wave are examined: coarse ($\lambda_0/5$); normal ($\lambda_0/10$); and fine ($\lambda_0/20$). For each resolution, the relation $c\Delta t = \frac{1}{2}\Delta$ was maintained. This relation is commonly used in two- and three-

Fig. 3. Variation o
di

pectively, the x-, y-,
vector; ω is the wave
he speed of light in
ing modeled.
l dispersion relation,
ion for a plane wave
ium is just

(13)

:e. Although, at first
nblance to the ideal
ow that (12) reduces
Δy, and Δz all go to
;ests that numerical
) any degree that is
ine-enough FD-TD

the dependence of
D-TD grid discretiz-
example the two-
)), assuming for sim-
$= \Delta y = \Delta$) and wave
with respect to the
$k_x = k \sin \alpha$). Then,
lifies to

$+\sin^2(\frac{1}{2}k \sin \alpha\, \Delta)$.

(14)

iiently solved for the
/ applying Newton's
cially convenient if Δ
ce wavelength.
using this procedure
of numerical phase
on angle in the FD-
d resolutions of the
ined: coarse ($\lambda_0/5$);
$_0/20$). For each reso-
was maintained. This
in two- and three-

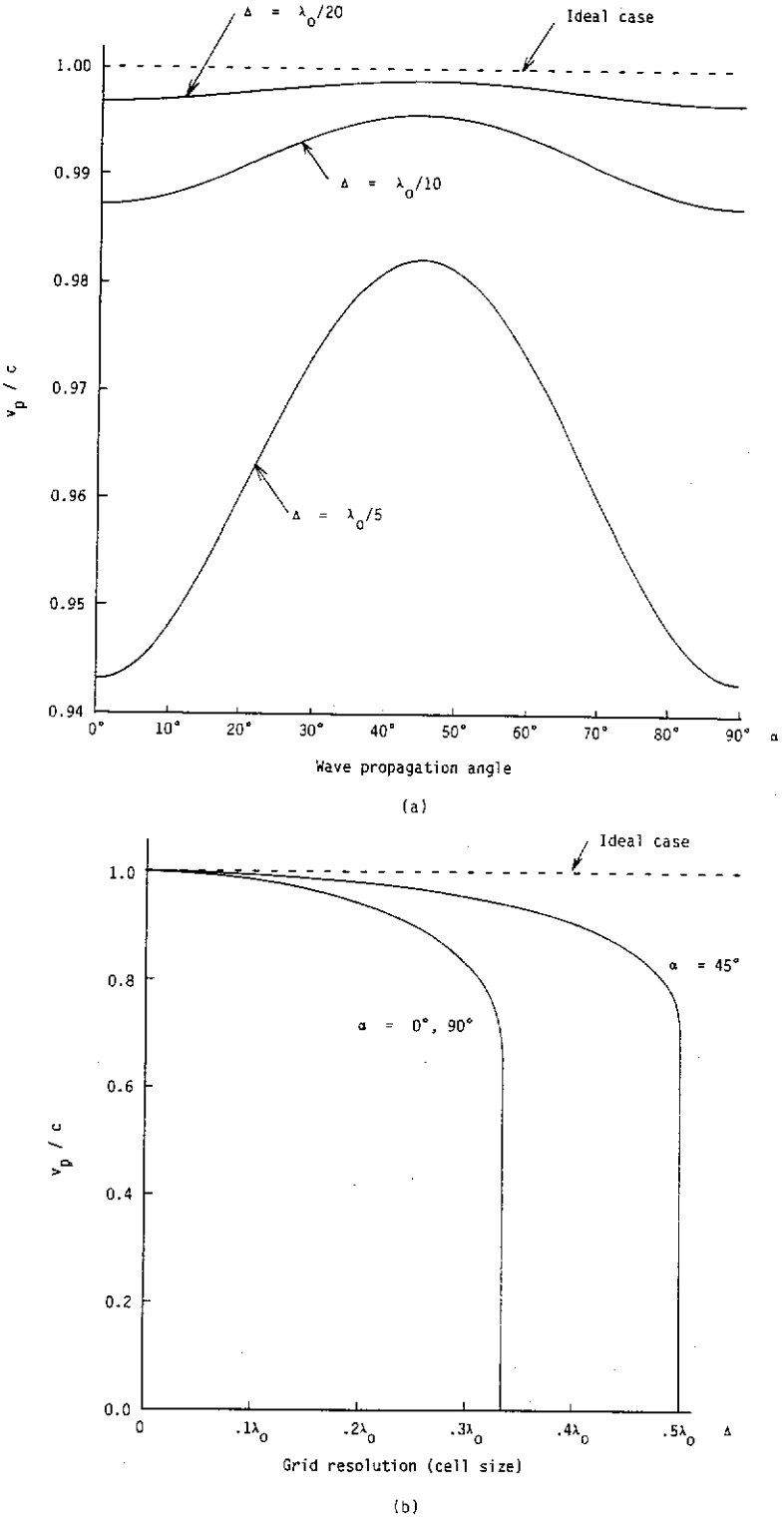

Fig. 3. Variation of FD-TD numerical wave phase velocity (dispersion): (a) with wave propagation angle in the grid for three different grid discretizations; (b) with grid resolution for three different wave propagation angles.

dimensional FD-TD codes to satisfy the numerical stability criterion of (11) with ample safety margin. From Fig. 3(a), it is seen that the numerical phase velocity is maximum at 45° (oblique incidence), and minimum at 0° and 90° (incidence along either Cartesian grid axis) for all grid resolutions. This represents a numerical anisotropy that is inherent in the Yee algorithm. However, the velocity error relative to the ideal case diminishes by approximately a 4:1 factor each time that the grid cell size is halved, so that the worst-case velocity error for the normal resolution case is only −1.3%, and only −0.31% for the fine resolution case.

Figure 3(b) graphs the variation of numerical phase velocity with grid resolution at the fixed incidence angles, 45° and 0° (90°). Again, the relation $c\Delta t = \frac{1}{2}\Delta$ was maintained for each resolution. Here, it is seen that the numerical phase velocity at each angle of incidence diminishes as the propagating wave is more coarsely resolved, eventually reaching a sharp threshold where the numerical phase velocity goes to zero and the wave can no longer propagate in the FD-TD grid. This represents a numerical low-pass filtering effect that is inherent in the Yee algorithm, wherein the wavelength of propagating numerical modes has a lower bound of 2 to 3 space cells, depending upon the propagation direction. As a result, FD-TD modeling of pulses having finite duration (and thus, infinite bandwidth) can result in progressive pulse distortion as higher spatial frequency components propagate more slowly than lower spatial frequency components, and very high spatial frequency components with wavelengths less than 2 to 3 cells are rejected. This numerical dispersion causes broadening of finite-duration pulses, and leaves a residue of high-frequency ringing on the trailing edges due to the relatively slowly propagating high-frequency components. From Figs. 3(a) and 3(b), we see that pulse distortion can be bounded by obtaining the Fourier spatial frequency spectrum of the desired pulse, and selecting a grid cell size so that the principal spectral components are resolved with at least 10 cells per wavelength. This would limit the spread of numerical phase velocities of the principal spectral components to less than 1%, regardless of the wave propagation angle in the grid.

In addition to numerical phase velocity anisotropy and pulse distortion effects, numerical dispersion can lead to pseudorefraction of propagating modes if the grid cell size is a function of position in the grid. Such variable-cell gridding would also vary the grid resolution of propagating numerical modes, and thereby perturb the modal phase velocity distribution. This would lead to nonphysical reflection and refraction of numerical modes at interfaces of grid regions having different cell sizes (even if these interfaces were located in free space), just as physical waves undergo reflection and refraction at interfaces of dielectric media having different indices of refraction. The degree of nonphysical refraction is dependent upon the magnitude and abruptness of the change of the modal phase velocity distribution, and can be estimated using conventional theory for wave refraction at dielectric interfaces.

We have stated that, in the limit of infinitesimal Δt and Δ, (12) reduces to (13), the ideal dispersion case. This reduction also occurs if Δt, Δ, and the direction of propagation are suitably chosen. For example, in a three-dimensional cubic lattice, reduction to the ideal dispersion case can be demonstrated for wave propagation along a lattice diagonal ($k_x = k_y = k_z = k/\sqrt{3}$) and $\Delta t = \Delta/c\sqrt{3}$ (exactly the limit set by numerical stability). Similarly, in a two-dimensional square grid, the ideal dispersion case can be demonstrated for wave propagation along a grid diagonal ($k_x = k_y = k/\sqrt{2}$) and $\Delta t = \Delta/c\sqrt{2}$ (again the limit set by numerical stability). Finally, in one dimension, the ideal case is obtained for $\Delta t = \Delta/c$ (again the limit set by numerical stability) for all propagating modes.

3.5. *Lattice zoning and plane wave source condition*

The numerical algorithm for Maxwell's curl equations defined by the finite-difference system reviewed above has a linear dependence upon the

components of the electromagnetic field vectors. Therefore, this system can be applied with equal validity to either the incident-field vector components, the scattered-field vector components, or the total-field vector components (the sum of incident plus scattered). Present FD-TD codes utilize this property to zone the numerical space lattice into two distinct regions, as shown in Fig. 4(a), separated by a rectangular virtual surface which serves to connect the fields in each region [11, 12].

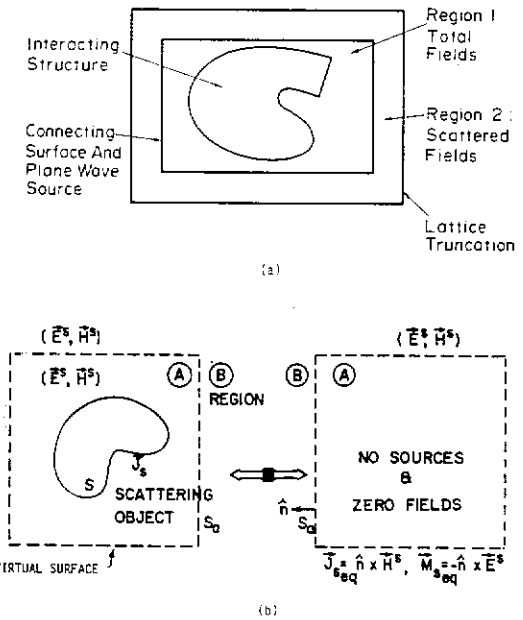

Fig. 4. Zoning of the FD-TD lattice: (a) total field and scattered field regions; (b) near-to-far field integration surface located in the scattered field region.

Region 1, the inner region of the FD-TD lattice, is denoted as the total-field region. Here, it is assumed that the finite-difference system for the curl equations operates on total-field vector components. The interacting structure of interest is embedded within this region.

Region 2, the outer region of the FD-TD lattice, is denoted as the scattered-field region. Here, it is assumed that the finite-difference system for the curl equations operates only on scattered-field vector components. This implies that there is no incident wave in Region 2. The outer lattice planes bounding Region 2, called the lattice truncation planes, serve to implement the free-space radiation condition (discussed in the next section) which simulates the field sampling space extending to infinity.

The total-field/scattered-field lattice zoning illustrated in Fig. 4(a) provides a number of key features which enhance the computational flexibility and dynamic range of the FD-TD method:

Arbitrary incident wave. The connecting condition provided at the interface of the inner and outer regions, which assures consistency of the numerical space derivative operations across the interface, simultaneously generates an arbitrary incident plane wave in Region 1 having a user-specified time waveform, angle of incidence, and angle of polarization. This connecting condition, discussed in detail in [10], almost completely confines the incident wave to Region 1 and yet is transparent to outgoing scattered wave modes which are free to enter Region 2.

Simple programming of inhomogeneous structures. The required continuity of total tangential E and H fields across the interface of dissimilar media is automatically provided by the original Yee algorithm if the media are located in a zone (such as Region 1) where total fields are time-marched. This avoids the problems inherent in a pure scattered-field code, where enforcement of the continuity of total tangential fields is a separate process requiring the incident field to be computed at all interfaces of dissimilar media, and then added to the values of the time-marched scattered fields at the interfaces. Clearly, computation of the incident field at numerous points along possibly complex, structure-specific loci is likely to be much more involved than computation of the incident field only along the simple connecting surface between Regions 1 and 2 (needed to implement the total-field/scattered-field zoning). The latter surface has a fixed locus that is independent of the shape or complexity of the interaction structure that is embedded in Region 1.

Wide computational dynamic range. Low levels of the total field in deep shadow regions or cavities of the interaction structure are computed directly by time-marching total fields in Region 1. In a pure scattered-field code, however, the low levels of total field are obtained by computing the incident field at each desired point, and then adding to the values of the time-marched scattered fields. Thus, it is seen that a pure scattered-field code relies upon near cancellation of the incident and scattered field components of the total field to obtain accurate results in deep shadow regions and cavities. An undesirable hallmark of this cancellation is contamination of the resultant low total-field levels by subtraction noise, wherein slight percentage errors in calculating the scattered fields result in possibly very large percentage errors in the residual total fields. By time-marching total fields directly, the zoned FD-TD code avoids subtraction noise in Region 1 and and achieves a computational dynamic range more than 30 dB greater than that for a pure scattered-field code.

Far-field response. The provision of a well-defined scattered-field region in the FD-TD lattice permits the near-to-far-field transformation illustrated in Fig. 4(b). The dashed virtual surface shown in Fig. 4(b) can be located along convenient lattice planes in the scattered-field region of Fig. 4(a). Tangential scattered E and H fields computed via FD-TD at this virtual surface can then be weighted by the free-space Green's function and then integrated (summed) to provide the far-field response and radar cross section (full bistatic response for the assumed illumination angle) [12–14]. The near-field integration surface has a fixed rectangular shape, and thus is independent of the shape or composition of the enclosed structure being modeled.

3.6. Radiation condition

A basic consideration with the FD-TD approach to solve electromagnetic wave interaction problems is that most computational domains of interest are ideally unbounded or "open". Clearly, no computer can store an unlimited amount of data, and therefore, the field computation zone must be limited in size. A suitable boundary condition on the outer perimeter of the computation zone must be used to simulate the extension of the computation zone to infinity. This boundary condition must be consistent with Maxwell's equations in that an outgoing vector scattered-wave numerical analog striking the lattice truncation must exit the lattice without appreciable nonphysical reflection, just as if the lattice truncation was invisible.

Now, the vector field components at the lattice truncation planes cannot be computed using the centered-differencing approach discussed earlier because of the assumed absence of known field data at points outside of the lattice truncation (which are needed to form the central differences). It has been shown that a suitable lattice truncation is provided by implementing a near-field radiation condition separately for each of the Cartesian tangential electric (or magnetic) vector components present in the truncation planes [11-13]. In FD-TD codes to date, the radiation condition used is a Pade (2,0) interpolant of the factored (one-way) wave equation [15, 16] as differenced in [11]. Higher-order Pade (2, 2) and Chebyshev (2, 2) interpolants are currently under study for numerical implementation in the FD-TD computer programs [17].

4. FD-TD modeling validations for electromagnetic wave scattering, two dimensions

Analytical and code-to-code validations have been obtained relative to FD-TD modeling of electromagnetic wave scattering for a wide variety of canonical two-dimensional structures. Both convex and re-entrant (cavity-type) shapes have been studied; and structure material compositions have included perfect conductors, homogeneous and inhomogeneous lossy dielectrics, and anisotropic dielectric and permeable media. Selected validations will be reviewed here.

4.1. Square meta

Here, we cons
ized plane wave
metal cylinder o
the side width o
grid cell size is
truncation (radi
uniform distanc
surface.

Figure 5 comp
the cylinder sur
computed using
benchmark cod
domain surface
(EFIE) via the n
MOM code assu
izes one-half o
divisions. The R
is taken as $\hat{n} \times$
vector at the cy
FD-TD value o
ponent in free s
cylinder surface
magnitude of the

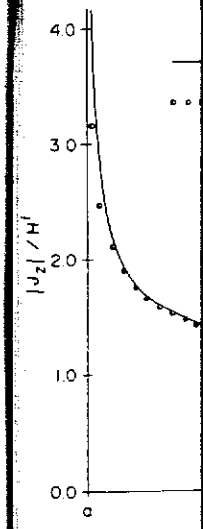

Fig. 5. Comparison
cur

4.1. Square metal cylinder, TM polarization [12]

Here, we consider the scattering of a TM-polarized plane wave obliquely incident upon a square metal cylinder of electrical size $k_0 s = 2$, where s is the side width of the cylinder. The square FD-TD grid cell size is set equal to $s/20$, and the grid truncation (radiation boundary) is located at a uniform distance of 20 cells from the cylinder surface.

Figure 5 compares the magnitude and phase of the cylinder surface electric current distribution computed using FD-TD to that computed using a benchmark code which solves the frequency-domain surface electric field integral equation (EFIE) via the method of moments (MOM). The MOM code assumes target symmetry and discretizes one-half of the cylinder surface with 84 divisions. The FD-TD computed surface current is taken as $\hat{\boldsymbol{n}} \times \boldsymbol{H}_{\tan}$, where $\hat{\boldsymbol{n}}$ is the unit normal vector at the cylinder surface, and $\boldsymbol{H}_{\tan}$ is the FD-TD value of the magnetic field vector component in free space immediately adjacent to the cylinder surface. From Fig. 5, we see that the magnitude of the FD-TD computed surface current agrees with the MOM solution to better than ±1% (±0.09 dB) at all comparison points more than 2 FD-TD cells from the cylinder corners (current singularities). The phase of the FD-TD solution agrees with the MOM solution to within ±3° at virtually every comparison point, including the shadow region.

4.2. Circular muscle-fat layered cylinder, TE polarization [18]

Here, we consider the penetration of a TE-polarized plane wave into a simulated biological tissue structure represented by a 15 cm radius muscle-fat layered cylinder. The inner layer (radius = 7.9 cm) is assumed to be comprised of muscle having a relative permittivity of 72 and conductivity of 0.9 S/m. The outer layer is assumed to be comprised of fat having a relative permittivity of 7.5 and conductivity of 0.48 S/m. An illumination frequency of 100 MHz is modeled, with the FD-TD grid cell size set equal to 1.5 cm (approximately 1/24 wavelength within the muscle). A stepped-edge (staircase) approximation of the circular layer boundaries is used.

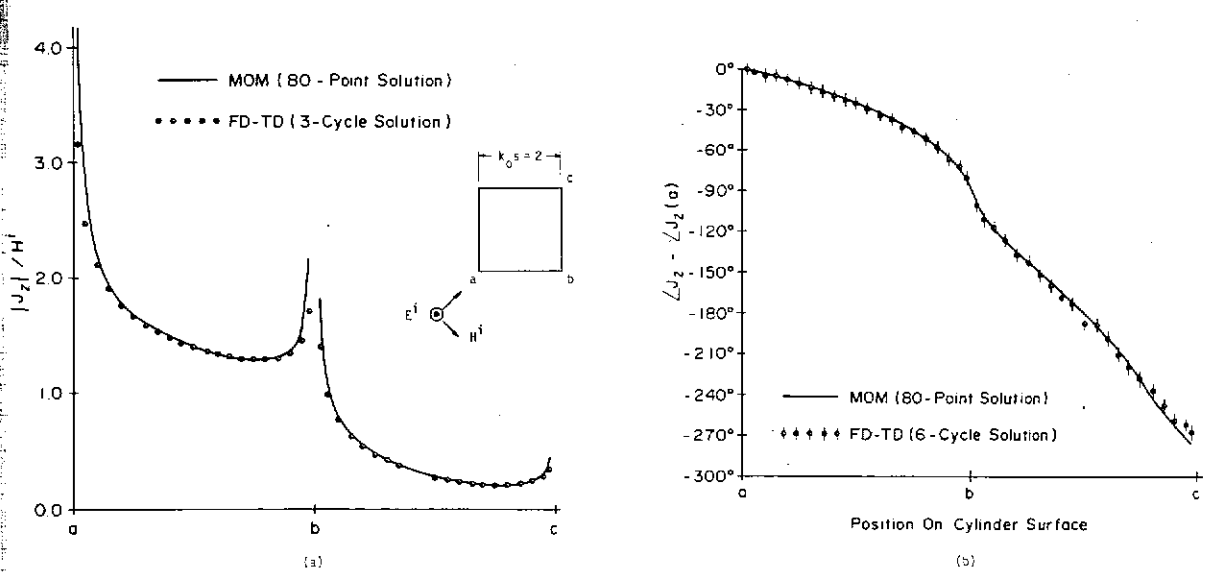

Fig. 5. Comparison of FD-TD and frequency-domain surface electric field integral equation results for longitudinal surface electric current distribution on a $k_0 s = 2$ square metal cylinder, TM case: (a) magnitude; (b) phase [12].

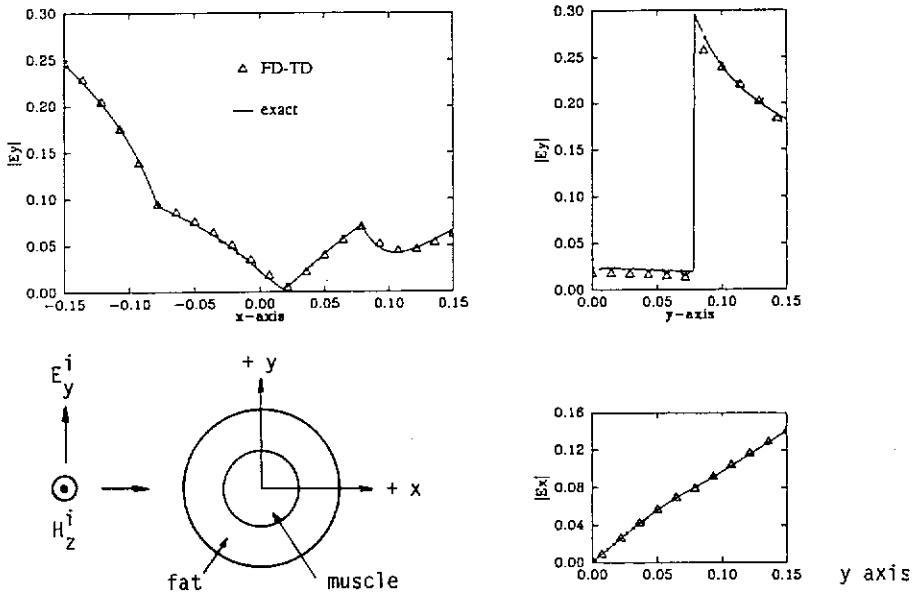

Fig. 6. Comparison of FD-TD and exact solutions for penetrating electric field vector components within a 15 cm radius, circular, muscle-fat layered cylinder, TE polarization, 100 MHz [18].

Figure 6, taken from [18], shows the analytical validation results for the magnitude of the penetrating electric field vector components along two cuts through the muscle-fat cylinder, one parallel to the direction of propagation of the incident wave, and one parallel to the incident electric field vector. The exact solution is obtained by summing sufficient terms of the eigenfunction expansion to assure convergence of the sum. Excellent agreement of the FD-TD and exact solutions is noted, even at jump discontinuities of the field (and at jump discontinuities of the slope of the field distribution) that occur at the layer boundaries. This fine agreement is observed despite the stepped-edge approximation of the circular layer boundaries.

4.3. Homogeneous, anisotropic, square material cylinder, TM polarization [19]

The ability to independently specify electrical permittivity and conductivity for each E vector component in the FD-TD lattice, and magnetic permeability and equivalent loss for each H vector component, leads immediately to the possibility of using FD-TD to model material structures having diagonalizable tensor electric and magnetic properties. No alteration of the basic FD-TD algorithm is required. The more complicated behavior associated with off-diagonal tensor components can also be modeled, in principle, with some algorithm complications [20].

Recent development of coupled, surface, combined-field integral equation (CFIE) theory for modeling electromagnetic wave scattering by arbitrary-shaped, two-dimensional, anisotropic material structures [19] has permitted detailed code-to-code validation studies of FD-TD anisotropic models. Figure 7 illustrates one such study. Here, the magnitude of the equivalent surface electric current induced by TM illumination of a square anisotropic cylinder is graphed as a function of position along the cylinder surface for both the FD-TD and CFIE models. The incident wave propagates in the $+y$-direction and has a $+z$-directed electric field. The cylinder has an electrical size $k_0 s = 5$, permittivity $\varepsilon_{zz} = 2$, and diagonal permeability tensor $\mu_{xx} = 2$ and $\mu_{yy} = 4$. For the

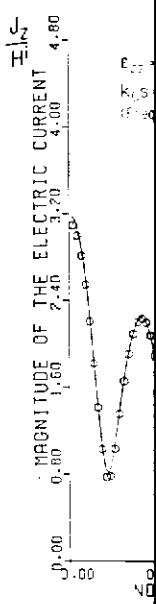

Fig. 7. Compar
combined-field
face electric cur

case shown,
to $s/50$, and
a uniform
surface.

From Fig
results agre
cylinder sur
cated series
noted at the
sharp local
Studies are
ics issue.

4.4. Circula TE and TM

A key fla
ducting stru

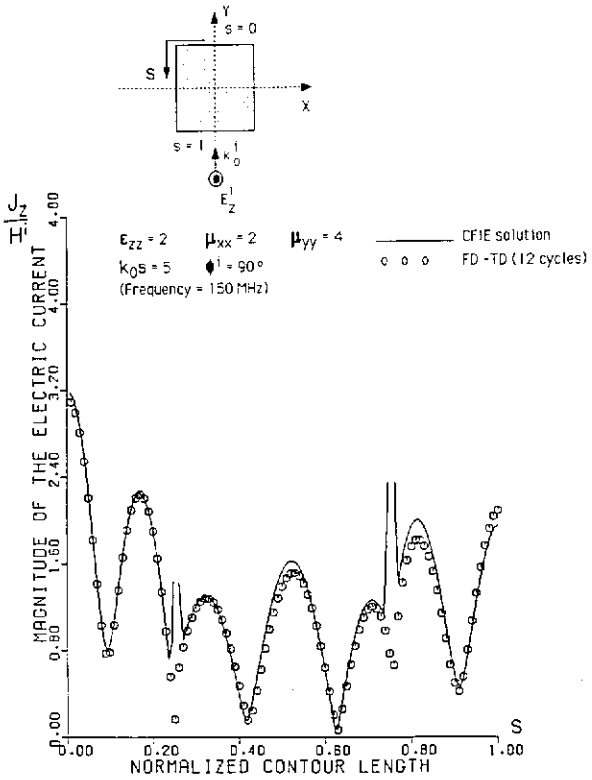

Fig. 7. Comparison of FD-TD and frequency-domain surface combined-field integral equation results for longitudinal surface electric current distribution on a $k_0 s = 5$ square anisotropic cylinder, TM case [19].

case shown, the FD-TD grid cell size is set equal to $s/50$, and the radiation boundary is located at a uniform distance of 20 cells from the cylinder surface.

From Fig. 7, we see that the FD-TD and CFIE results agree very well almost everywhere on the cylinder surface, despite the presence of a complicated series of peaks and nulls. Disagreement is noted at the cylinder corners where CFIE predicts sharp local peaks, but FD-TD predicts local nulls. Studies are continuing to resolve this corner physics issue.

4.4. *Circular metal cylinder, conformally modeled, TE and TM polarization*

A key flaw in previous FD-TD models of conducting structures with smooth curved surfaces has been the need to use stepped-edge (staircase) approximations of the actual structure surface. Although not a serious problem for modeling wave penetration and scattering for low-Q metal cavities, recent FD-TD studies have shown that stepped approximations of curved walls and aperture surfaces can shift center frequencies of resonant responses by 1% to 2% for Q factors of 30 to 80, and can possibly introduce spurious nulls [21]. In the area of scattering, the use of stepped surfaces has limited application of FD-TD for modeling the important class of targets where surface roughness, exact curvature, and dielectric or permeable loading is important in determining the radar cross section.

Recently, two different types of FD-TD conformal surface models have been proposed and examined for two-dimensional problems:

(1) *Faraday's Law contour path models* [22]. These preserve the basic Cartesian grid arrangement of field components at all space cells except those adjacent to the structure surface. Space cells adjacent to the surface are deformed to conform with the surface locus. Slightly modified time-stepping expressions for the magnetic field components adjacent to the surface are derived from the integral form of Faraday's Law implemented around the perimeters of the deformed cells.

(2) *Stretched, conforming mesh models* [23, 24]. These employ available numerical mesh generation schemes to construct non-Cartesian grids which are continuously and globally stretched to conform with smoothly shaped structures. Time-stepping expressions are either adapted from the Cartesian FD-TD case [23] or obtained via analogy to the computational fluid dynamics formalism [24].

Research is ongoing for each of these types of conformal surface models. Key questions include: ease of mesh generation; suppression of numerical artifacts such as instability, dispersion, pseudorefraction, and subtraction noise limitation of computational dynamic range; coding complexity; and computer execution time. (See also the paper by Madsen and Ziolkowski in this issue.)

The accuracy of the Faraday's Law contour path models for smoothly curved structures subjected to TE and TM illumination is illustrated in Figs. 8(a) and 8(b) respectively. Here, a moderate-resolution Cartesian FD-TD grid (having 1/20 wavelength cell size) is used to compute the azimuthal or longitudinal electric current distribution on the surface of a $k_0a = 5$ circular metal cylinder. For both polarizations, the contour path FD-TD model achieves an accuracy of 1.5% or better at most surface points relative to the exact series solution. Running time for the conformal FD-TD model is essentially the same as for the old staircase FD-TD model since only a few H components immediately adjacent to the target surface require a slightly modified time-stepping relation.

4.5. *Flanged metal open cavity [25]*

Here, we consider the interaction of a TM-polarized plane wave obliquely incident upon a flanged metal open cavity. The open cavity is formed by a flanged parallel-plate waveguide having a plate spacing, a, of 1 m, short-circuited by a terminating plate located at a distance, d, of 1 m from the aperture. At the assumed illumination frequency of 382 MHz, $k_0a = k_0d = 8$, and only the first two TE waveguide modes propagate within the open cavity. An oblique angle of incidence, $\alpha = 30°$, is assumed for this case.

Figure 9 compares the magnitude and phase of the penetrating electric field within the cavity $\frac{2}{3}$ m from the aperture computed using FD-TD to that computed using a cavity modal expansion and OSRC [25]. Good agreement is seen. Figure 10 shows a similar comparison for the bistatic radar cross section due to the induced aperture field distribution. Again, good agreement is noted.[1]

[1] It should be noted that the results obtained using the cavity modal expansion and OSRC represent a good approximation, but not a rigorous solution.

4.6. *Relativistically vibrating mirror, oblique incidence [26]*

Analytical validations have been recently obtained for FD-TD models of reflection of a monochromatic plane wave by a perfectly conducting surface either moving at a uniform relativistic velocity or vibrating at a frequency and amplitude large enough so that the surface attains relativistic speeds [26]. The FD-TD approach of [26] is novel in that it does not require a system transformation where the conducting surface is at rest. Instead, the FD-TD grid is at rest in the laboratory frame, and the computed field solution is given directly in the laboratory frame. This is accomplished by implementing the proper relativistic boundary conditions for the fields at the surface of the moving conductor.

Figure 11 shows results for one of the more interesting problems of this type modeled so far, that of oblique plane wave incidence on an infinite vibrating mirror. This case is much more complicated than the normal incidence case, in that it has no closed-form solution. An analysis presented in the literature [27] writes the solution in an infinite-series form using plane-wave expansions, where the unknown coefficients in the series are solved numerically. This analysis serves as the basis of comparison for the FD-TD model results for the time variation of the scattered field envelope at points near the mirror.

Since it is difficult to model exactly an infinite plane mirror in a finite two-dimensional grid, a long, thin, rectangular perfectly-conducting slab is used as the mirror model, as shown in Fig. 11(a). Relativistic boundary conditions for the fields are implemented on the front and back sides of the slab. The other two sides, parallel to the velocity vector, are insensitive to the motion of the slab, and therefore no relativistic boundary conditions are required there. To minimize the effect of edge diffraction, the slab length is carefully selected so that the slab appears to be infinite in extent at observation point, P, during a well-defined early-time response when the edge effect has not yet

Fig. 8. Compariso

propagated to
vide appreciab
[27], only the
11(b), we see g

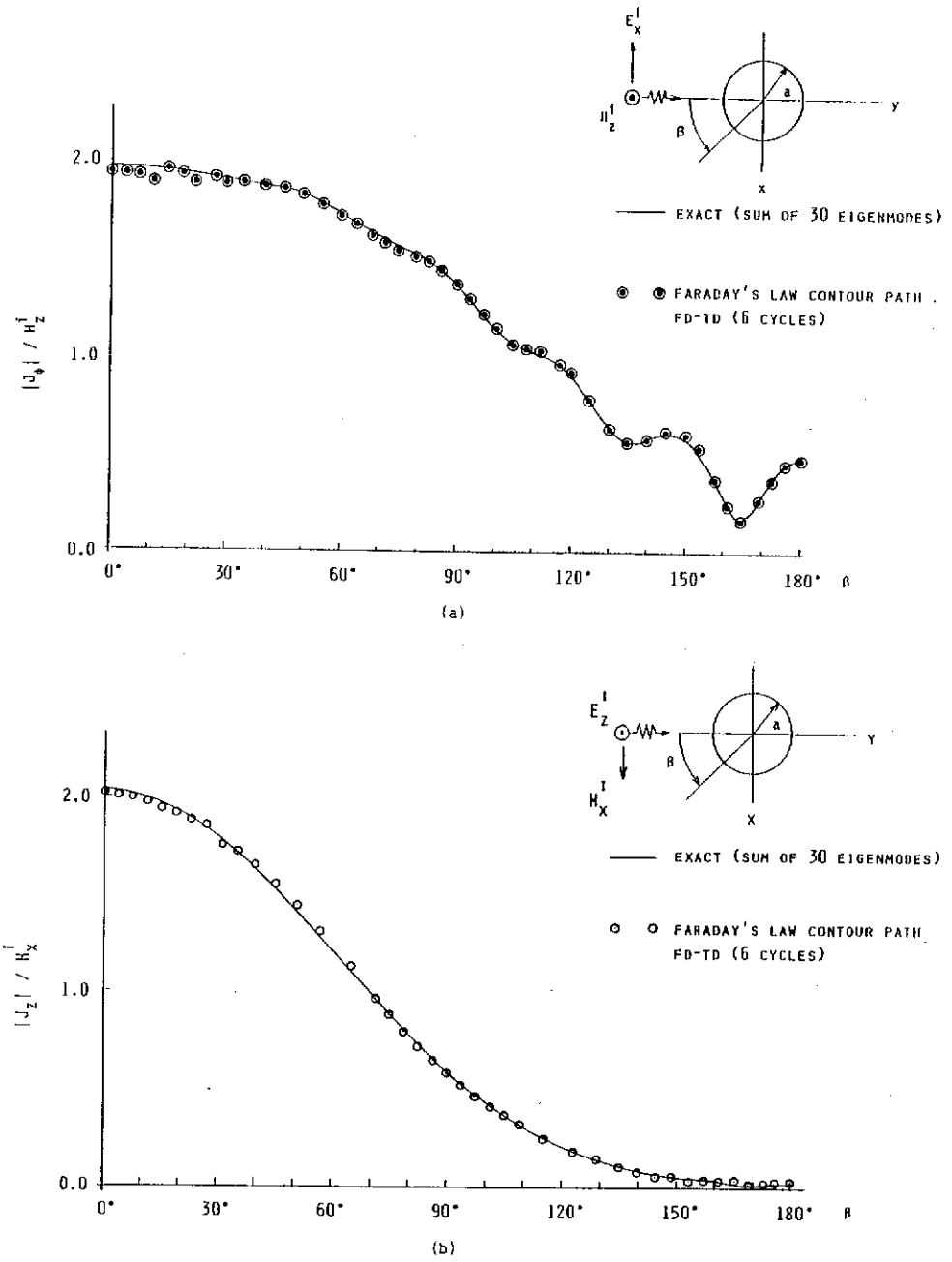

Fig. 8. Comparison of Faraday's Law contour-path FD-TD and exact solutions for surface electric current distribution on a $k_0 a = 5$ circular metal cylinder: (a) TE case, azimuthal current; (b) TM case, longitudinal current [22].

propagated to *P*. Since the TM case does not provide appreciably different results than the TE case [27], only the TE case is considered. From Fig. 11(b), we see good agreement between the FD-TD and analytical results obtained from [27] for the envelope of the scattered E field vs. time for an incident angle of 30°, peak mirror speed 20% that of light, and observation points $z/d = -5$ and

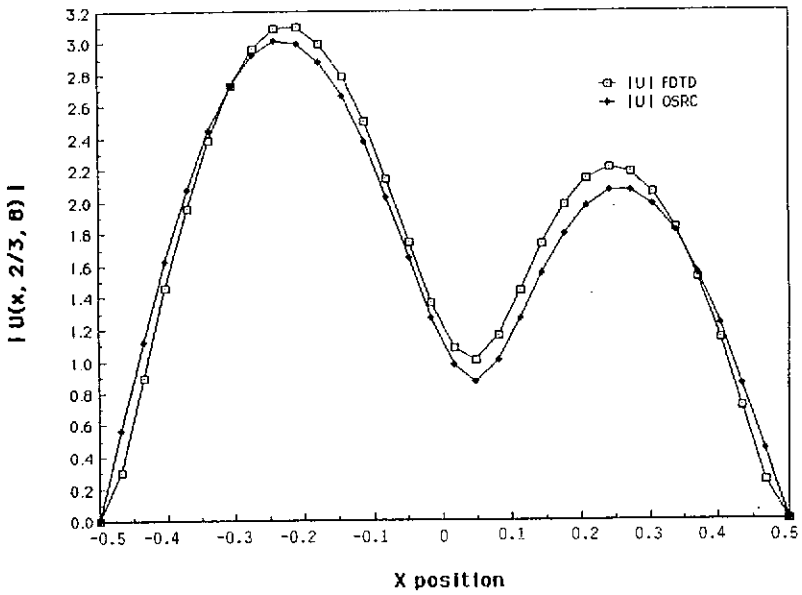

(a)

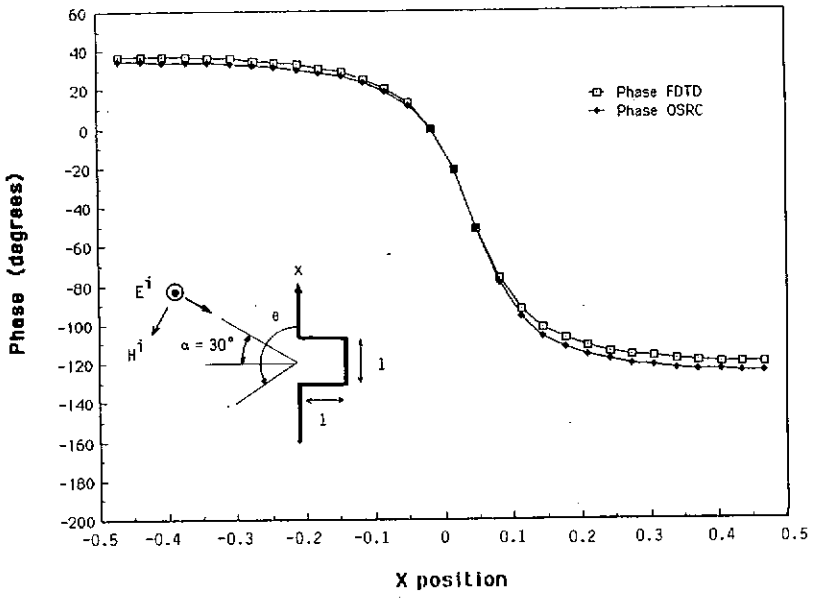

(b)

Fig. 9. Comparison of FD-TD and frequency-domain modal/OSRC approximate solution for the penetrating electric field distribution $\frac{2}{3}$ meter within the flanged open cavity: (a) magnitude; (b) phase [25].

Fig. 10. Compa

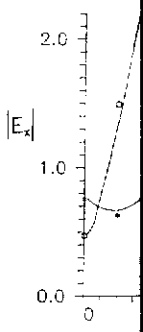

Fig. 11. Compa
envelope of the
matic plane wav
at a 30° oblique
solutions at t

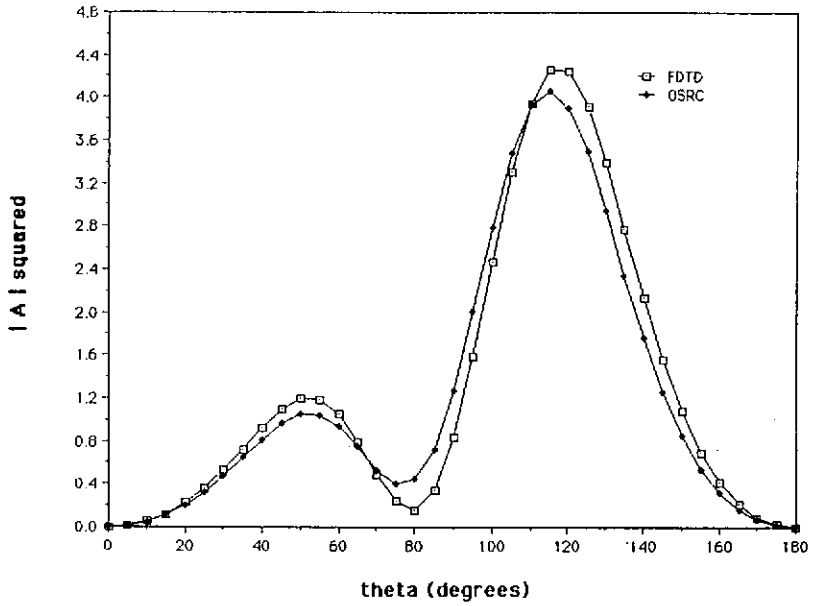

Fig. 10. Comparison of FD-TD and frequency-domain modal/OSRC approximate solution for the bistatic radar cross section due to the induced aperture field distribution of the flanged open cavity [25].

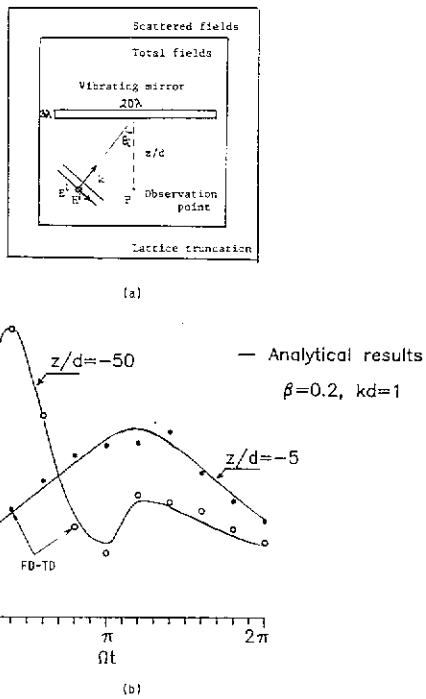

Fig. 11. Comparison of FD-TD and analytical results for the envelope of the scattered electric field vs. time for a monochromatic plane wave illuminating a relativistically vibrating mirror at a 30° oblique angle: (a) problem geometry; (b) comparative solutions at two distances from the mirror surface [26].

$z/d = -50$, where $kd = 1$. Similar agreement is found for an even more oblique angle, 60° [26]. This agreement is satisfying since the action of the relativistically vibrating mirror is so complicated, generating a reflected wave having a spread both in frequency and spatial reflection angle, as well as evanescent modes.

5. FD-TD modeling validations for electromagnetic wave scattering, three dimensions

Analytical, code-to-code, and experimental validations have been obtained relative to FD-TD modeling of electromagnetic wave scattering for a wide variety of canonical three-dimensional structures, including cubes, flat plates, and crossed plates. Selected validations will be reviewed here.

5.1. Metal cube, broadside incidence [13]

Results are now shown for the FD-TD computed surface electric current distribution on a metal cube subject to plane-wave illumination at broadside incidence. The electric current distribution is com-

pared to that computed by solving a frequency-domain surface EFIE using a standard triangular surface-patching MOM code [13]. It is shown that a very high degree of correspondence exists between the two sets of predictive data.

The detailed surface current study involves a cube of electrical size $k_0 s = 2$, where s is the side width of the cube. For the FD-TD model, each face of the cube is spanned by 400 square cells (20×20), and the radiation boundary is located at a uniform distance of 15 cells from the cube surface. For the MOM model, each face of the cube is spanned by either 18 triangular patches or 32 triangular patches (to test the convergence of the MOM model). Comparative results for surface current are graphed along two straight-line loci along the cube: $\overline{abcd}$, which is in the plane of the incident magnetic field; and $\overline{ab'c'd}$, which is in the plane of the incident electric field.

Figure 12 compares the FD-TD and MOM results for the magnitude and phase of the surface current along $\overline{ab'c'd}$. The FD-TD values agree with the high-resolution MOM data to better than ±2.5% (±0.2 dB) at all comparison points. Phase agreement for the same sets of data is better than ±1°. (The low-resolution MOM data have a phase anomaly in the shadow region.) In Fig. 13, comparably excellent agreement is obtained along $\overline{abcd}$, but only after incorporation of an edge-correction term in the MOM code [28] to enable it to properly model the current singularities at the cube corners, b and c.

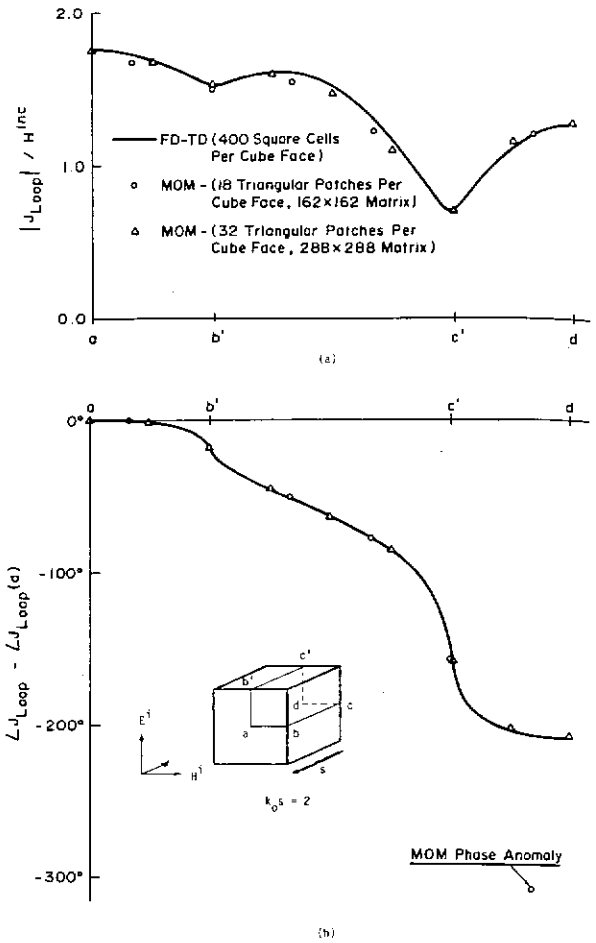

Fig. 12. Comparison of FD-TD and frequency-domain surface electric field integral equation results for surface electric current distribution along the E-plane locus, $\overline{ab'c'd}$, of the $k_0 s = 2$ metal cube: (a) magnitude; (b) phase [13].

5.2. *Flat conducting plate, multiple monostatic looks [14, 20]*

We next consider a 30 cm × 10 cm × 0.65 cm flat conducting plate target. At 1 GHz, where the plate spans 1 wavelength, a comparison is made between FD-TD and MOM results for the monostatic radar cross section (RCS) vs. look-angle azimuth (keeping a fixed elevation angle), as shown in Fig. 14(a). Here, the FD-TD model uses a uniform cell size of 0.625 cm ($\lambda_0/48$), forming the plate by $48 \times 16 \times 1$ cells. The radiation boundary is located at a uniform distance of only 8 cells from the plate surface. For the MOM model, study of the convergence of the computed broadside RCS indicates that the plate thickness must be accounted by using narrow side patches, and the space resolution of each surface patch should be finer than approximately 0.2 wavelength. As a result, the MOM model forms the plate by $10 \times 3 \times 1$ divisions, yielding a total of 172 triangular surface patches. Figure 14(a) shows excellent agreement between the two models (within about ±0.2 dB).

At 9 GHz, the plate spans 9 wavelengths, and the use of the MOM model is virtually precluded.

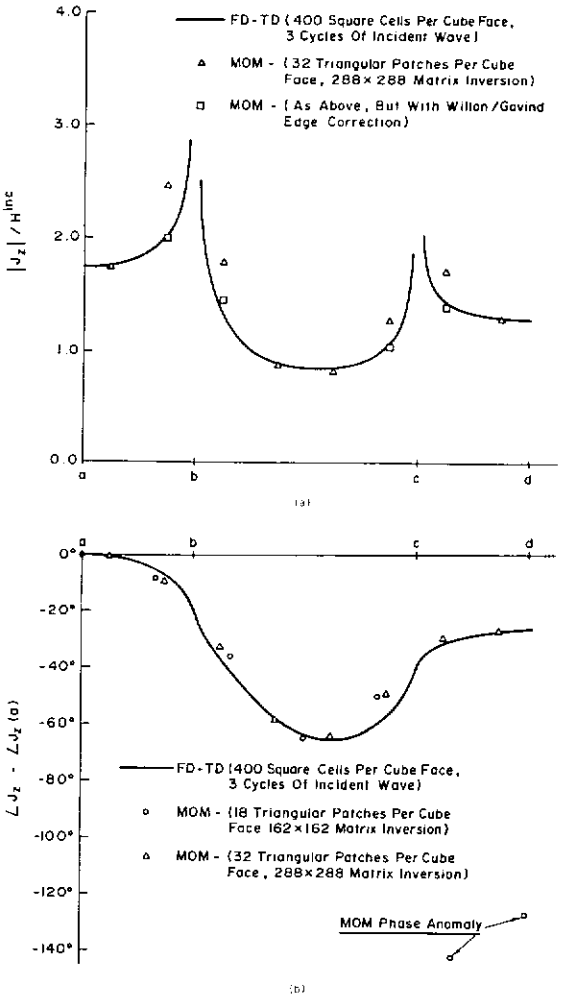

Fig. 13. Comparison of FD-TD and frequency-domain surface electric field integral equation results for surface electric current distribution along the H-plane locus, $\overline{abcd}$, of the $k_0 s = 2$ metal cube: (a) magnitude; (b) phase [13].

If we follow the convergence guidelines discussed above, the plate would require approximately $50 \times 15 \times 1$ divisions to properly converge, yielding a total of 3260 triangular surface patches, and requiring the generation and inversion of a 4890×4890 complex-valued system matrix. On the other hand, FD-TD remains feasible for the plate at 9 GHz. Choosing a uniform cell size of 0.3125 cm ($\lambda_0/10.667$), the plate is formed by $96 \times 32 \times 2$ cells. With the radiation boundary again located only 8 cells from the plate surface, the overall lattice size is $112 \times 48 \times 18$, containing 580,608 unknown field components (real numbers). Figure 14(b) shows excellent agreement between the FD-TD results and measurements of the monostatic RCS vs. look angle performed in the anechoic chamber facility operated by SRI International. The observed agreement is within about 1 dB and 1° of look angle. As will be seen next, this level of agreement is maintained for more complicated targets having corner reflector properties.

5.3. T-shaped conducting target, multiple monostatic looks [14, 20]

We last consider the monostatic RCS pattern of a T-shaped target comprised of two flat conducting plates electrically bonded together. The main plate has the dimensions 30 cm × 10 cm × 0.33 cm, and the bisecting fin has the dimensions 10 cm × 10 cm × 0.33 cm.[2] The illumination is a 9.0 GHz plane wave at 0° elevation angle and TE polarization relative to the main plate. Thus, the main plate spans 9.0 wavelengths. Note that look-angle azimuths between 90° and 180° provide substantial corner reflector physics, in addition to the edge diffraction, corner diffraction, and other effects found for an isolated flat plate.

For this target, the FD-TD model uses a uniform cell size of 0.3125 cm ($\lambda_0/10.667$), forming the main plate by $32 \times 96 \times 1$ cells and the bisecting fin by $32 \times 32 \times 1$ cells. With the radiation boundary again located only 8 cells from the target's maximum surface extensions, the overall lattice size is $48 \times 112 \times 48$, containing 1,548,288 unknown field components (212.6 cubic wavelengths). Starting with zero-field initial conditions, 661 time steps are used, equivalent to 31 cycles of the incident wave at 9.0 GHz.

Figure 15 compares the FD-TD predicted monostatic RCS values at 32 key look angles between 0° and 180° with measurements performed by SRI International. These look angles are selec-

[2] The center line of the "bisecting" fin is actually positioned 0.37 cm to the right of the center line of the main plate. This is accounted for in the FD-TD model.

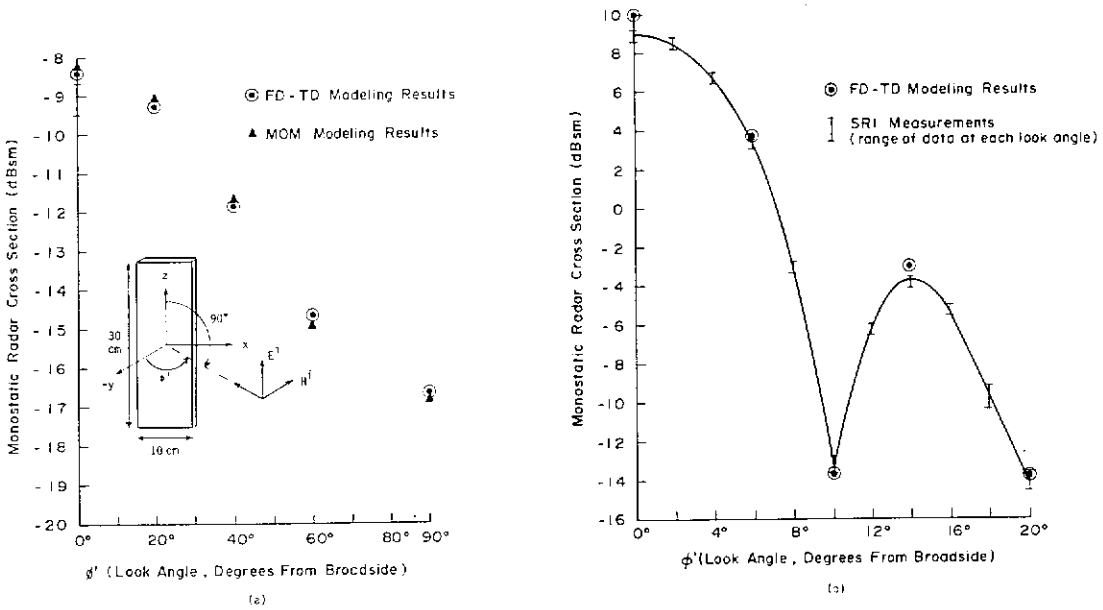

Fig. 14. Validation of FD-TD results for the monostatic radar cross section of a rectangular, flat conducting plate: (a) versus frequency-domain surface electric field integral equation results at 1 GHz (plate size = $1 \times \frac{1}{3}$ wavelengths); (b) versus anechoic chamber measurements at 9 Ghz (plate size = 9×3 wavelengths) [14, 20].

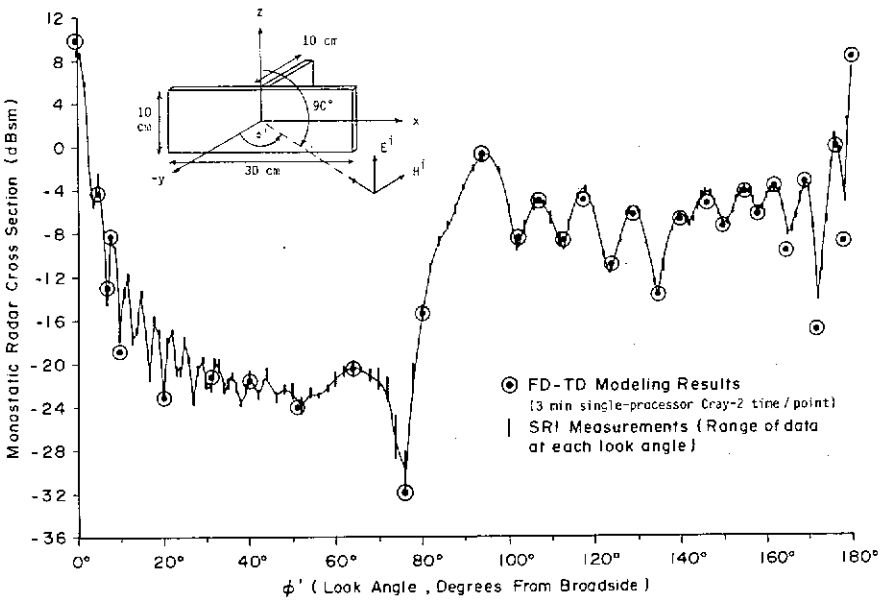

Fig. 15. Comparison of FD-TD modeling predictions with anechoic chamber measurements of monostatic radar cross section for a T-shaped conducting target at 9 GHz (target span = $9 \times 3 \times 3$ wavelengths) [14, 20].

ted to define the major peaks and nulls of the monostatic RCS pattern. It is seen that the agreement is again excellent: in amplitude, within about 1 dB over a total RCS-pattern dynamic range of 40 dB; and in azimuth, within 1° in locating the peaks and nulls of the RCS pattern. Note especially the fine agreement for look-angle azimuths greater than 90°, where there is a pronounced corner reflector effect.

6. FD-TD modeling validations for electromagnetic wave penetration and coupling, two and three dimensions

6.1. Penetration models for narrow slots and lapped joints in thick screens

The physics of electromagnetic wave transmission through narrow slots and lapped joints in shielded enclosures must be accurately understood to permit good engineering design of equipment to meet specifications for performance concerning electromagnetic pulse, lightning, high-power microwaves, electromagnetic interference and compatibility, undesired radiated signals, and RCS. In many cases, slots and joints can have very narrow gaps filled by air, oxidation films, or layers of anodization. Joints can be simple (say, two metal sheets butted together); more complex (a lapped or "furniture" joint); or even more complex (a threaded screw-type connection with random points of metal-to-metal contact, depending upon the tightening). Extra complications arise from the possibility of electromagnetic resonances within the joint, either in the transverse or longitudinal (depth) direction.

Clearly, to make any headway with this complicated group of problems using the FD-TD approach, it is necessary to develop and validate FD-TD models which can simulate the geometric features of generic slots and joints. Since a key geometric feature is likely to be the narrow gap of the slot or joint relative to one FD-TD space cell, it is important to understand how subcell gaps can be efficiently modeled.

Three different types of FD-TD subcell models have been proposed and examined for modeling narrow slots and joints:

(1) *Equivalent slot loading* [29]. Here, rules are set to define an equivalent permittivity and permeability in a slot formed by a single-cell gap to effectively narrow the gap to the desired degree.

(2) *Subgridding* [30]. Here, the region within the slot or joint is provided with a sufficiently fine grid. This grid is properly connected to the coarser grid outside of the slot.

(3) *Faraday's Law contour path model* [31]. Here, space cells adjacent to and within the slot or joint are deformed to conform with the surface locus (in a manner similar to the conformal curved surface model). Slightly modified time-stepping expressions for the magnetic field components in these cells are derived from the integral form of Faraday's Law implemented about the perimeters of the deformed cells.

The accuracy of the Faraday's Law contour path model for narrow slots and joints is illustrated in Figs. 16 and 17 by direct comparison of the computed gap electric field distribution against high-resolution numerical benchmarks. Figure 16 models a 0.1 wavelength thick conducting screen which extends 0.5 wavelength to each side of a straight slot which has a gap of 0.025 wavelength. Broadside TE illumination is assumed. Three types of predictive data are compared: (1) the low-resolution (0.1 λ_0) FD-TD model using the contour path approach to treat the slot as a $\frac{1}{4}$-cell gap; (2) a high-resolution (0.025 λ_0) FD-TD model treating the slot as a 1-cell gap; and (3) a very-high-resolution frequency-domain EFIE model, solved via MOM (having 0.0025 λ_0 sampling in the slot) which treats the slotted screen as a pure scattering geometry. From Fig. 16, we see that there is excellent agreement between all three sets of predictive data in both magnitude and phase. Of particular interest is the ability of the low-resolution FD-TD model, using the contour path approach, to accurately compute the peak electric field in the slot.

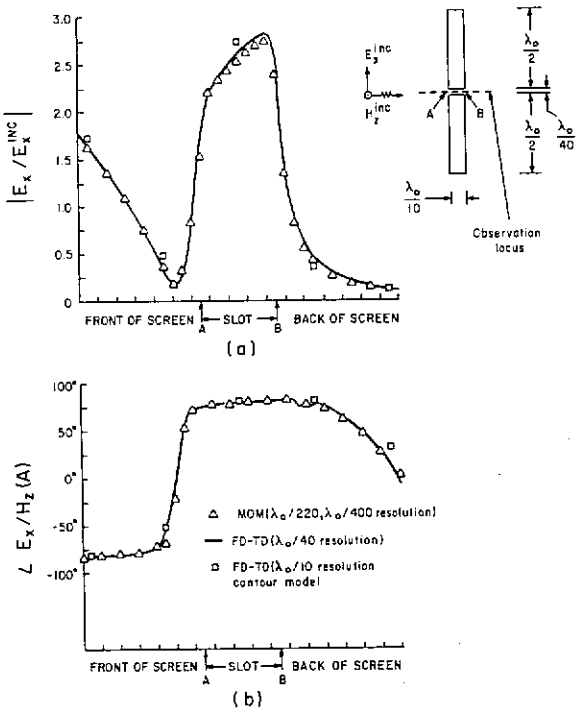

Fig. 16. Comparison of FD-TD and frequency-domain surface electric field integral equation results for the gap electric field distribution in a slotted conducting screen, straight slot case, TE illumination: (a) magnitude; (b) phase [31].

Figure 17 shows the geometry of a U-shaped lapped joint which was selected for detailed study of path-length (depth) power transmission resonances. The U shape of the joint permits adjustment of the overall joint path length without disturbing the positions of the input and output ports at *A* and *F*. A uniform gap of 0.025 wavelength is assumed, as is a screen thickness of 0.3 wavelength

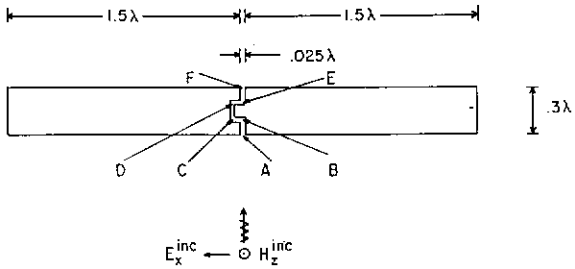

Fig. 17. Geometry of U-shaped lapped joint in a conducting screen, TE illumination (shown to scale) [31].

and width of 3 wavelengths. Figure 18 compares the gap electric field distribution within the joint as computed by: (1) a low-resolution ($0.09\,\lambda_0$) contour path FD-TD model treating the gap as 0.28 cell; and (2) a high-resolution ($0.025\,\lambda_0$) FD-TD model treating the gap as 1 cell. The total path length $\overline{ABCDEF}$ within the lapped joint is adjusted to equal 0.45 wavelength, which provides a sharp power transmission peak to the shadow side of the screen. From Fig. 18, we see a very good agreement between the low- and high-resolution FD-TD models, even though this is a numerically stressful resonant penetration case.

An implication of these results is that coarse ($0.1\,\lambda_0$) FD-TD gridding can be effectively used to model the fine-grained physics of wave penetration through subcell slots and joints if simple algorithm modifications are made in accordance with the contour path approach. This can substantially reduce computer resource requirements and coding complexity for FD-TD models of complex structures, without sacrificing appreciable accuracy in the results.

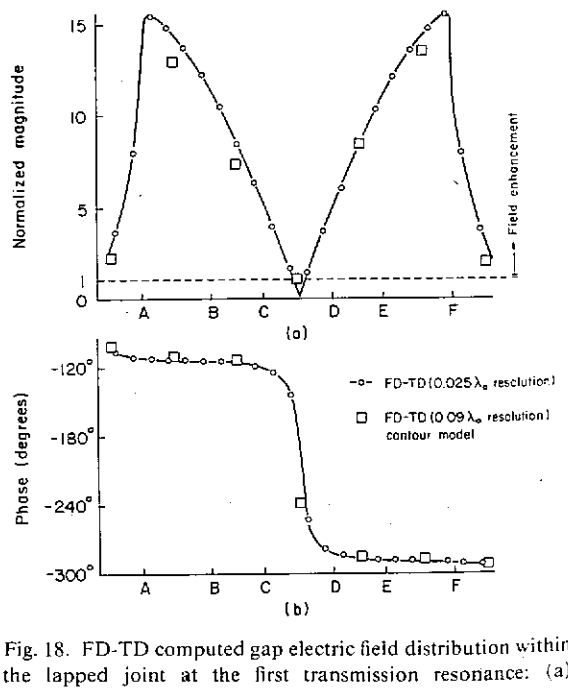

Fig. 18. FD-TD computed gap electric field distribution within the lapped joint at the first transmission resonance: (a) $|E_{gap}/E_{inc}|$; (b) $\angle E_{gap}/H_z(A)$ [31].

18 compares
thin the joint
tion ($0.09\ \lambda_0$)
ıg the gap as
$0.025\ \lambda_0$) FD-
The total path
ıped joint is
hich provides
o the shadow
we see a very
nd high-resol-
iis is a numeri-
case.
is that coarse
ctively used to
ve penetration
nple algorithm
ance with the
ı substantially
ients and cod-
ls of complex
appreciable

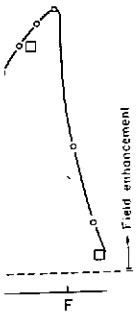

D-TD (0.025 λ_0 resolution)
FD-TD (0.09 λ_0 resolution)
contour model

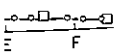

ld distribution within
sion resonance: (a)
A) [31].

6.2. Coupling models for wires and wire bundles

In equipment design for threats represented by electromagnetic pulse, high-power microwaves, and electromagnetic interference, understanding electromagnetic wave coupling to wires and cable bundles located within shielding enclosures is a problem that is complementary to that of wave penetration through apertures of the shield (such as narrow slots and joints). Similar to the narrow slot problem, a key dimension of the interacting structure, in this case the wire or bundle diameter, may be small relative to one FD-TD space cell. Thus, it is important to understand how thin, subcell, wires and bundles can be efficiently modeled if FD-TD is to have much application to coupling problems.

Two different types of FD-TD subcell models have been proposed and examined for modeling thin wires:

(1) *Equivalent inductance* [32]. Here, an equivalent inductance is defined for a wire within a space cell, permitting a lumped-circuit model of the wire to be set up and computed in parallel with the field solution.

(2) *Faraday's Law contour path model* [21]. Here, space cells adjacent to the wire are deformed to conform with the surface locus (in a manner similar to the conformal curved surface model). $1/r$ singularities of the azimuthal magnetic field and radial electric field are assumed to exist within the deformed cells. Slightly modified time-stepping expressions for the azimuthal magnetic field components in these cells are derived from the integral form of Faraday's Law implemented around the perimeter of the deformed cells.

The accuracy of the Faraday's Law contour path model for thin wires in free space is illustrated in Figs. 19(a) and 19(b). Figure 19(a) graphs the scattered azimuthal magnetic field at a fixed distance of 1/20 wavelength from the center of an infinitely long wire having a radius ranging between 1/30,000 and 1/30 wavelength. TM illumination is assumed. We see that there is excellent agreement between the exact series solution and

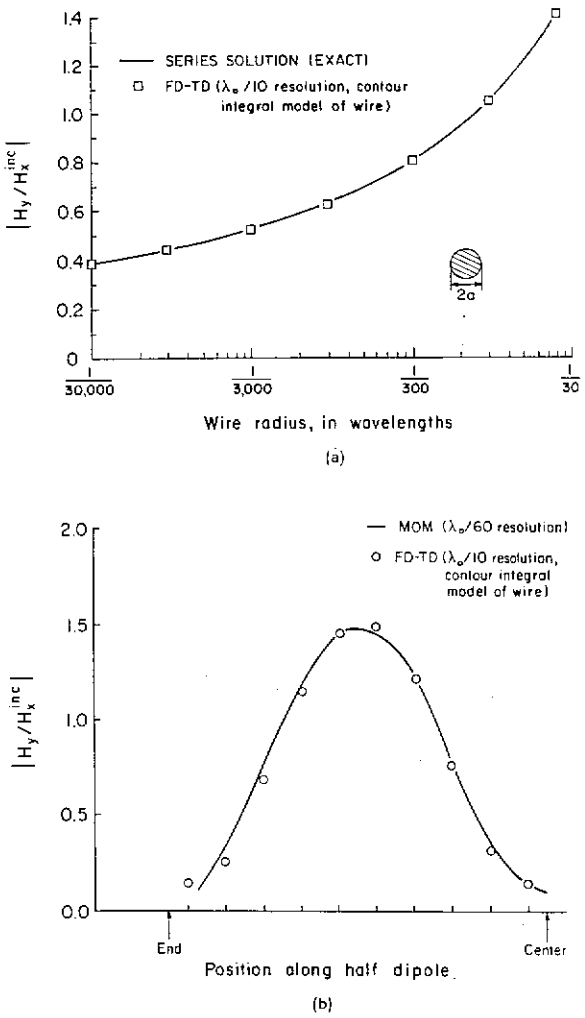

Fig. 19. Validation studies for the Faraday's Law contour path FD-TD model for thin wires in free space: (a) comparison of FD-TD and exact solutions for the scattered azimuthal magnetic field at a fixed distance of 1/20 wavelength from the center of an infinitely long wire (as a function of wire radius); (b) comparison of FD-TD and MOM results for the scattered azimuthal magnetic field distribution along a 2.0 wavelength (antiresonant) wire of radius 1/300 wavelength [21].

the low-resolution ($0.1\ \lambda_0$) FD-TD contour path model over the entire 3-decade range of wire radius. Figure 19(b) graphs the scattered azimuthal magnetic field distribution along a 2.0 wavelength (antiresonant) wire of radius 1/300 wavelength. Broadside TM illumination is assumed, and the field is observed at a fixed distance of 1/20 wavelength from the wire center. We see that there

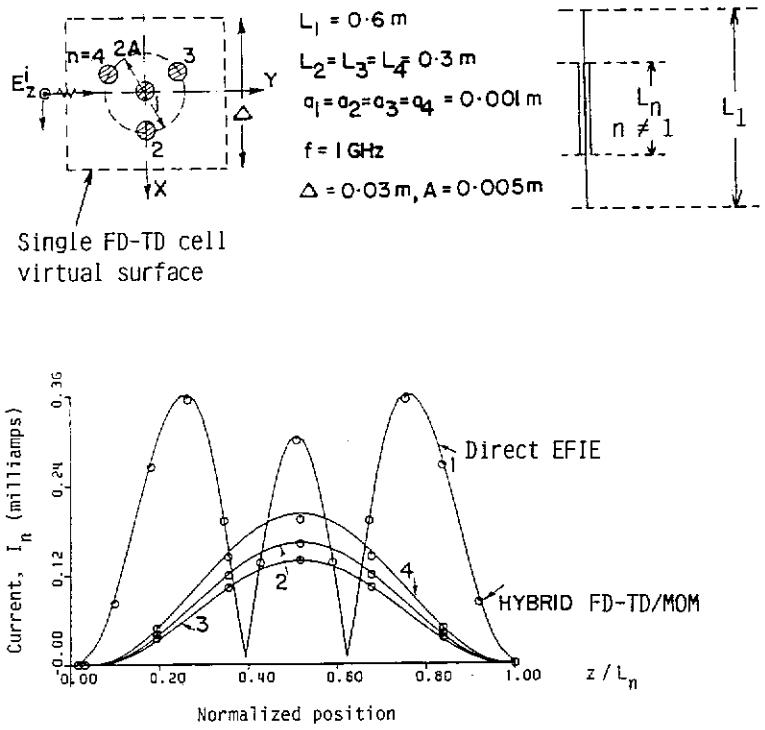

Fig. 20. Comparison of hybrid FD-TD/MOM modeling predictions with direct frequency-domain electric field integral equation results for induced currents on a wire bundle [21].

is excellent agreement between a frequency-domain EFIE (MOM) solution sampling the wire current at 1/60 wavelength increments, and the low-resolution ($0.1\,\lambda_0$) FD-TD contour path model.

The FD-TD contour path model can be extended to treat thin wire bundles, as well as single wires. Figure 20 shows the code-to-code validation results for the induced currents on a bundle comprised of 4 wires, where 3 are of equal length. Here, a wire of length 60 cm (2.0 wavelengths) is assumed to be at the center of the bundle, and three parallel wires of length 30 cm (1.0 wavelength) are assumed to be located at 120° angular separations on a concentric circle of radius 5 mm (1/60 wavelength). The radii of all wires in the bundle are equal and set to 1 mm (1/300 wavelength). The assumed excitation is in free space, provided by a 1 GHz broadside TM plane wave. Following the technique of [21], the bundle is replaced by a single wire having varying equivalent radius corresponding to the three sections along the bundle axis. The physics of the single wire of varying equivalent radius is incorporated in a low-resolution ($0.1\,\lambda_0$) FD-TD contour path model, as discussed above. The FD-TD model is then run to obtain the tangential E and H fields at a virtual surface conveniently located at the cell boundary containing the equivalent wire (shown as a dashed line in Fig. 20). These fields are then utilized as excitation to obtain the currents induced on the individual wires of the original bundle. This last step is performed by setting up an EFIE and solving via MOM. Figure 20 shows an excellent correspondence between the results of the hybrid FD-TD/MOM procedure described above and the usual direct EFIE (MOM) solution for the induced current distribution on each wire of the bundle.

The hybrid FD-TD/MOM procedure for modeling thin wire bundles is most useful when the

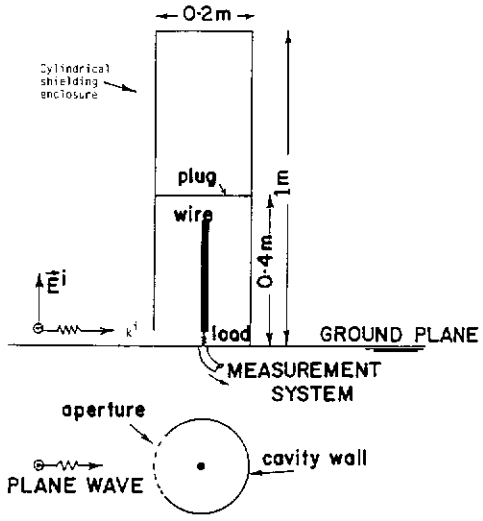

Fig. 21. Geometry of the cylindrical metal shielding enclosure and internal wire or wire-pair [21].

bundle is located within a shielding enclosure. Figures 21 and 22 show the geometry and test results for such a model involving the variation of induced load current with illumination frequency for a single wire and a wire-pair located at the center of a cylindrical metal enclosure. The enclosure is 1.0 m high, 0.2 m in diameter, and referenced to a large metal ground plane. Approximate plane wave illumination is provided by an electrically-large conical monopole referenced to the same ground plane. Wave penetration into the interior of the enclosure is through a circumferential slot aperture (12.5 cm arc length, 1.25 cm gap) at the ground plane. For the cases studied, an internal shorting plug is located 40 cm above the ground plane. For the single-wire test, a wire of length 30 cm and radius 0.495 mm is centered within the interior and connected to the ground plane with a lumped 50-ohm load. For the wire-pair test, parallel wires of these dimensions are located 1 cm apart, with one wire shorted to the ground plane and the other connected to the ground plane with a lumped 50-ohm load. All results are normalized to a 1 V/m incident wave electric field.

From Fig. 22, we see that there is a good correspondence between the measured and numerically modeled wire load current for both test cases. The two-wire test proved to be especially challenging since the observed Q factor of the coupling response (center frequency divided by the half-power bandwidth) is quite high, about 75. Indeed, it is found that the FD-TD code has to be stepped through as many as 80 cycles to approximately reach the sinusoidal steady state for illumination frequencies near the resonant peak [21]. However, substantially fewer cycles of time-stepping are needed away from the resonance, as indicated in the figure.

7. Use of FD-TD for modeling very complex three-dimensional structures

Two characteristics of FD-TD cause it to be very promising for numerical modeling of electromagnetic wave interactions with very complex objects: (1) Dielectric and permeable media can be specified independently for each electric and magnetic field vector component in the three-dimensional volume being modeled. Since there may be tens of millions of such vector components in large FD-TD models, inhomogeneous media of enormous complexity can be specified in principle. (2) The required computer resources for this type of detailed volumetric modeling are dimensionally low, only of order N, where N is the number of space cells in the FD-TD lattice.

The emergence of supercomputers has recently permitted FD-TD to be seriously applied to a number of very complex electromagnetic wave interaction problems. Two of these will now be briefly reviewed.

7.1. UHF wave penetration into a missile seeker section [6, 33]

Here, FD-TD is applied to model the penetration of an axially incident 300 MHz plane wave into a metal-coated missile guidance section. The FD-TD model, shown in Fig. 23, contains the following elements: (1) magnesium fluoride

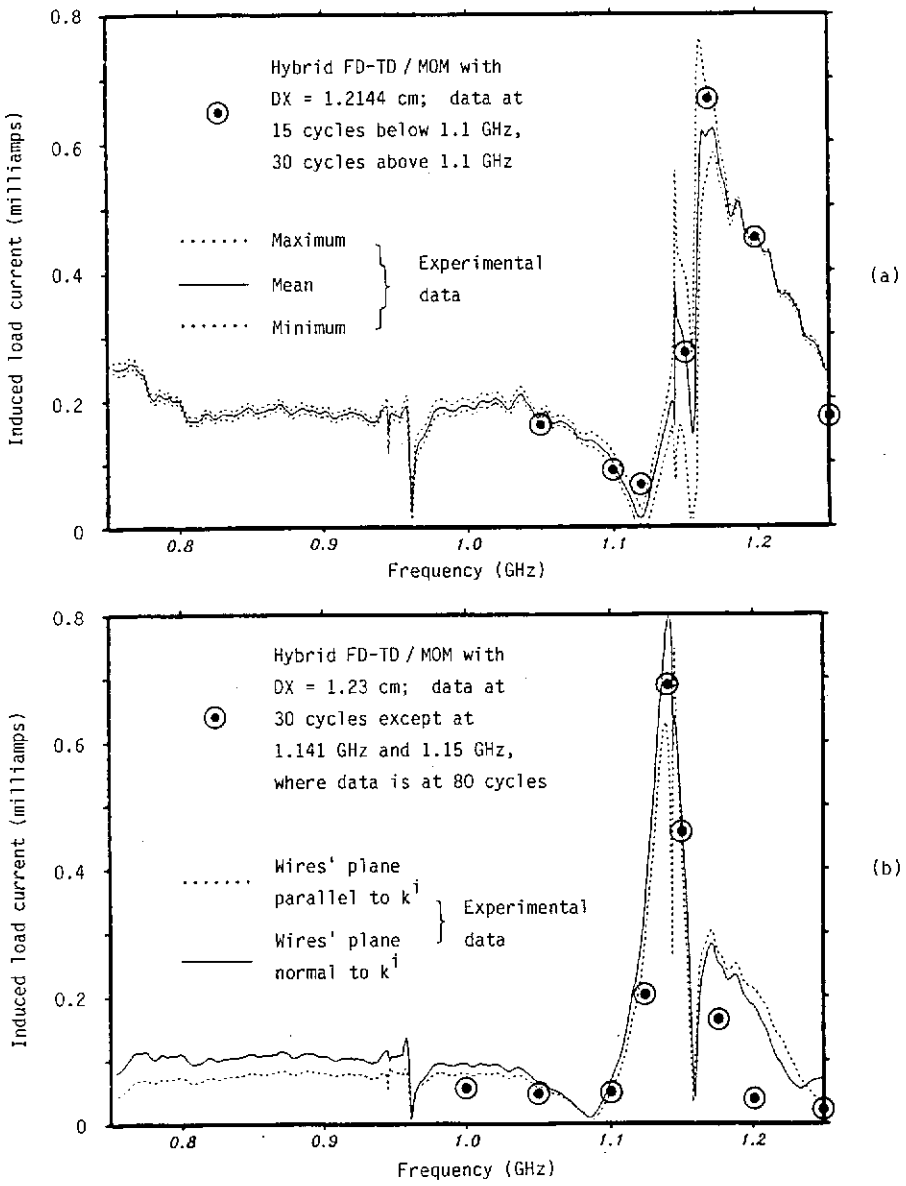

Fig. 22. Comparison of hybrid FD-TD/MOM modeling predictions with experimental data for induced load current: (a) single wire in shielding enclosure; (b) wire pair in shielding enclosure [21].

infrared dome; (2) circular nose aperture; (3) circumferential sleeve-fitting aperture 23 cm aft (loaded with fiberglass); (4) head-coil assembly; (5) cooled detector unit with enclosing phenolic ring; (6) pre-amp can; (7) wire bundle connecting the detector unit to the pre-amp can; (8) wire bundle connecting the pre-amp can to the metal backplane; and (9) longitudinal metal support rods. The fiberglass structure of the nose cone and its metalization are approximated in a stepped-surface manner, as is the infrared dome.

For this structure, the FD-TD model uses a uniform cell size of $\frac{1}{3}$ cm ($\lambda_0/300$), with an overall lattice size of $24\times100\times48$ cells containing

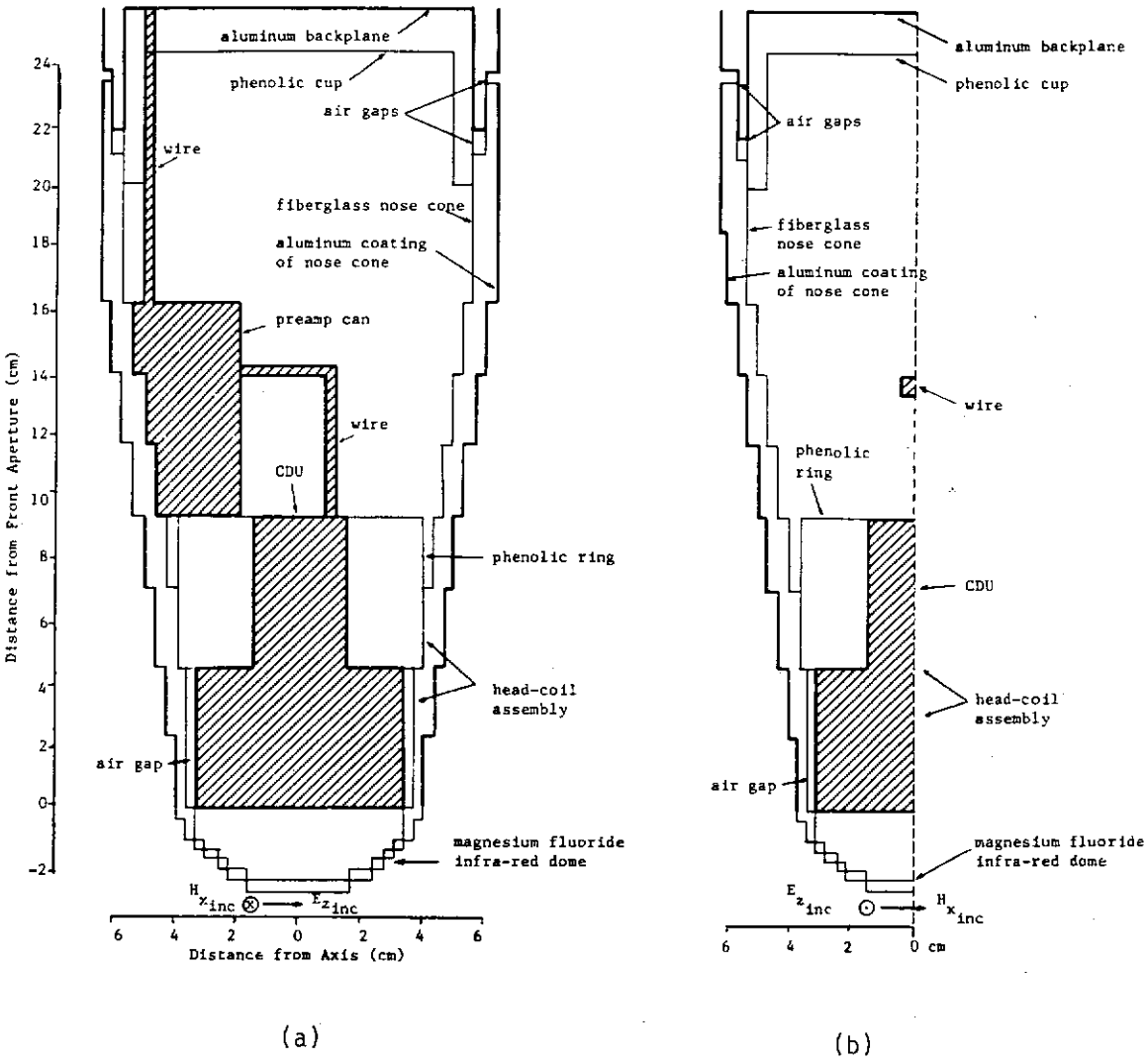

Fig. 23. FD-TD model of the missile seeker section, showing component materials: (a) at the vertical symmetry plane; (b) at the horizontal observation plane [6, 33].

690,000 unknown field components. (A single symmetry plane is used, giving an effective lattice size of $48 \times 100 \times 48$.) The model is run for 1800 time steps, equivalent to 3.0 cycles of the incident wave at 300 MHz.

Figure 24 plots contour maps of the FD-TD computed field vector components at the symmetry plane of the model. An important observation is that the simulated wire bundles connecting the cooled detector unit, pre-amp can, and metal backplane are paralleled by high-level magnetic field contours (Fig. 24(b)). This is indicative of substantial, uniform current flow along each bundle. Such current flow would generate locally a magnetic field looping around the wire bundle which, when "cut" by the symmetry plane, shows up as parallel field contours spaced equally on each side of the bundle. Using a simple Ampere's Law argument, the common-mode bundle currents can be calculated, thus obtaining a key transfer function

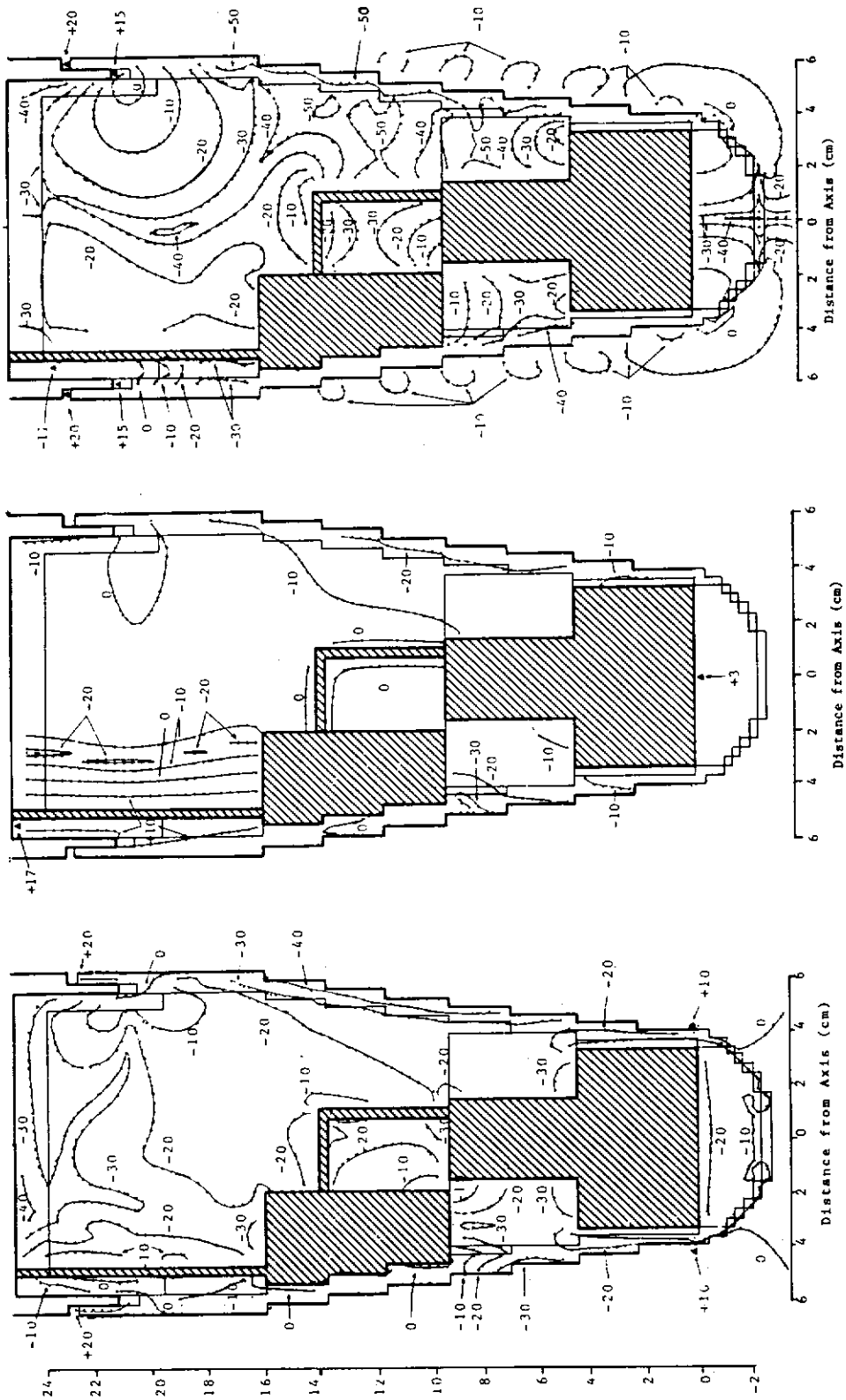

Fig. 24. FD-TD computed contour maps of penetrating field vector components in the vertical symmetry plane of the missile seeker section: (a) E_z; (b) H_x; (c) E_x [6, 33].

between free-field incident UHF plane wave power density and coupled wire currents [33]. As stated earlier, this information is useful for studies of vulnerability of electronic systems to upset due to both natural and man-made electromagnetic phenomena.

Although this missile seeker model was composed to demonstrate the capability of FD-TD to map fields penetrating into a complex structure having multiple apertures and realistic internal engineering details, it should be understood that the full bistatic radar cross section pattern of the structure is available as a byproduct with virtually no additional effort. Further, with the $\frac{1}{3}$ cm space resolution used, the FD-TD radar cross section model would be useful up to 9 GHz.

7.2. *Whole-body human dosimetry at VHF and UHF frequencies [34, 35]*

Here, FD-TD is applied to model the penetration of plane waves at VHF and UHF frequencies into the entire human body. Directly exploiting the ability of FD-TD to model media inhomogeneities down to the space-cell level, highly realistic three-dimensional FD-TD tissue models of the complete body have been constructed. Specific electrical parameters are assigned to each of the electric field vector components at the 16,000 to 40,000 space cells comprising the body model. Assignments are based upon detailed cross-section tissue maps of the body (as obtained via cadaver studies available in the medical literature), and cataloged measurements of tissue dielectric properties. Uniform FD-TD space resolutions as fine as 1.3 cm throughout the entire human body have proven feasible with the Cray-2.

Figure 25, taken from [35], shows the FD-TD computed contour maps of the specific absorption rate (SAR) distribution along horizontal cuts through the head and liver of the three-dimensional inhomogeneous man model. In Fig. 25(a), the incident wave has a power density of 1 mW/cm^2 at 350 Mhz, while in Fig. 25(b), the incident wave has the same power density but is at 100 MHz. These contour maps illustrate the high level of detail of local features of the SAR distribution that is possible via FD-TD modeling for highly realistic tissue models.

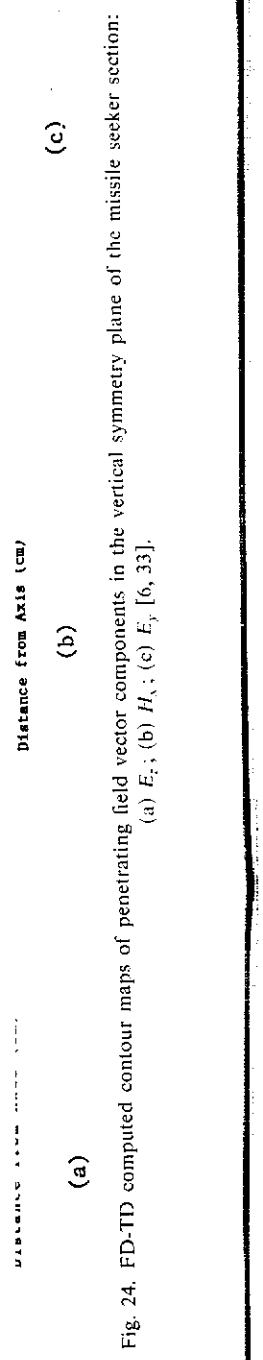

Fig. 24. FD-TD computed contour maps of penetrating field vector components in the vertical symmetry plane of the missile seeker section: (a) E_z; (b) H_x; (c) E_y [6, 33].

8. FD-TD microstrip and microwave circuit models

Recently, FD-TD modeling has been extended to provide detailed characterizations of microstrips, resonators, finlines, and two-dimensional microwave circuits. In [36], FD-TD is used to calculate the dispersive characteristics of a typical microstrip on a gallium arsenide substrate. A Gaussian pulse excitation is used, and the effective dielectric constant and characteristic impedance vs. frequency is efficiently obtained over a broad frequency range via Fourier transform of the time-domain field response.

In [37], FD-TD is first used to obtain resonant frequencies of several three-dimensional cavities loaded by dielectric blocks. Next, the resonant frequency of a finline cavity is computed. Last, the resonant frequencies of a microstrip cavity on anisotropic substrate are obtained, and the dispersion characteristics of the microstrip used in the cavity are calculated. FD-TD modeling results are compared primarily to those obtained using the transmission line matrix (TLM) approach, and the two methods are found to give practically the same results. (See also the paper by Johns in this issue [pp. 597-610].)

In [38], a modified version of FD-TD is presented which provides central-difference time-stepping expressions for distributions of voltage and surface current density along arbitrary-shaped two-dimensional microwave circuits. This approach is quite different from that of [36, 37], which utilize the original volumetric field sampling concept for FD-TD. As a result, the method of [38] requires fewer unknowns to be solved, and avoids the need for a radiation boundary condition. However, an auxiliary condition is required to describe the loading effects of the fringing fields

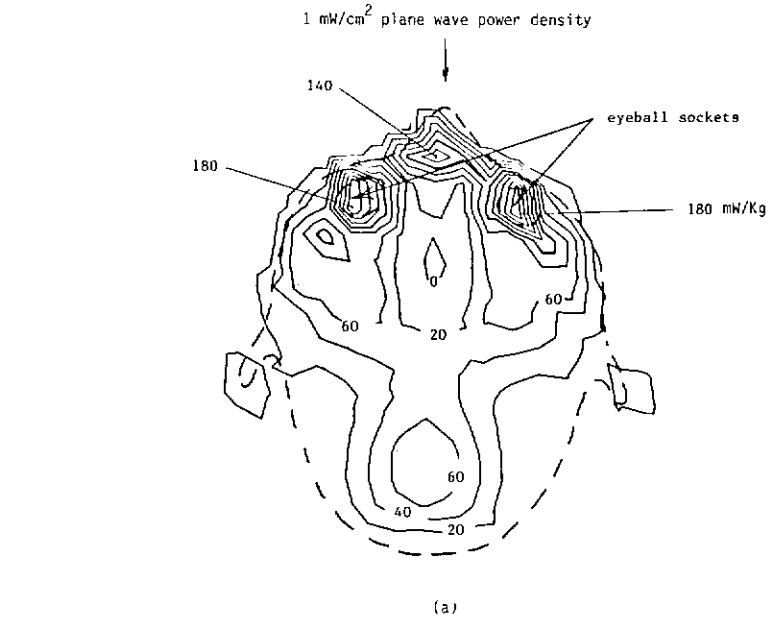

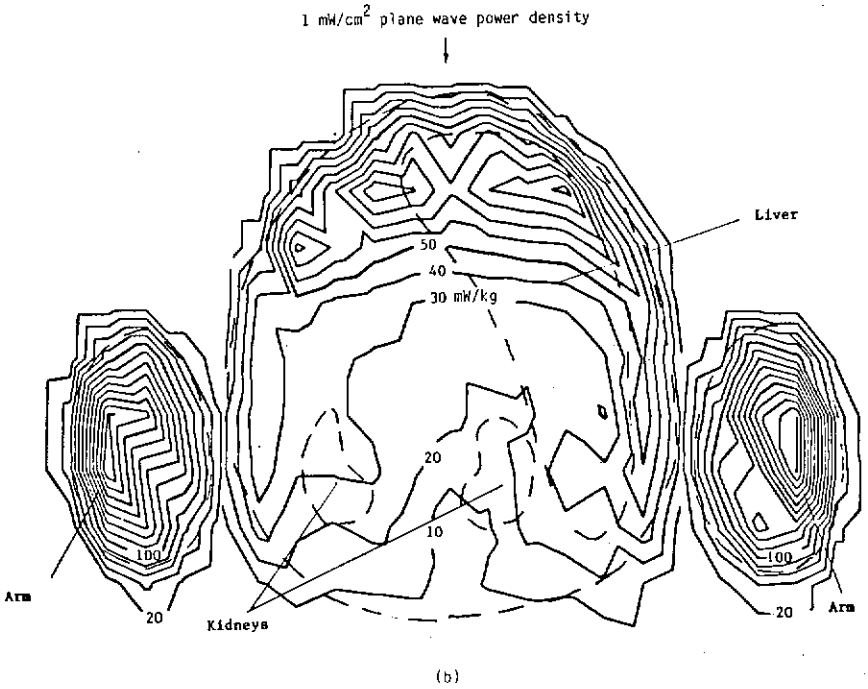

Fig. 25. FD-TD computed contour maps of the specific absorption rate due to penetrating electromagnetic fields within a highly realistic, three-dimensional model of the entire human body: (a) along a horizontal cut through the head at 350 MHz; (b) along a horizontal cut through the liver at 100 MHz [35].

at the edge
Figure 26,
computed
frequency
The ring ci
has an inner
substrate re
permeability
connected to
The broadba

Fig. 26. Compar

at the edges of the microstrip conducting paths. Figure 26, taken from [38], shows the FD-TD computed S-parameter, $|S_{21}|$, as a function of frequency for a two-port microstrip ring circuit. The ring circuit, gridded as shown in the figure, has an inner radius of 4 mm, outer radius of 7 mm, substrate relative permittivity of 10 and relative permeability of 0.93 (simulating duroid), and is connected to two 50-ohm lines making a 90° angle. The broadband response of the circuit is obtained using a single FD-TD run for an appropriate pulse excitation, followed by Fourier transformation of the desired response time-domain waveform. From Fig. 26, we see good agreement of the predicted and measured circuit response over the 2–12 GHz frequency band and a dynamic range of about 30 dB. Reference [38] concludes that the application of its FD-TD approach to arbitrarily-shaped microstrip circuits is encouraging, but more work is needed to determine the modeling limitations,

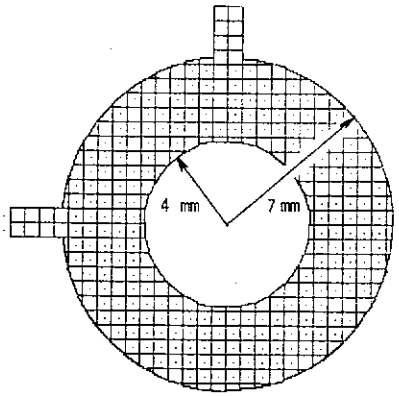

(a)

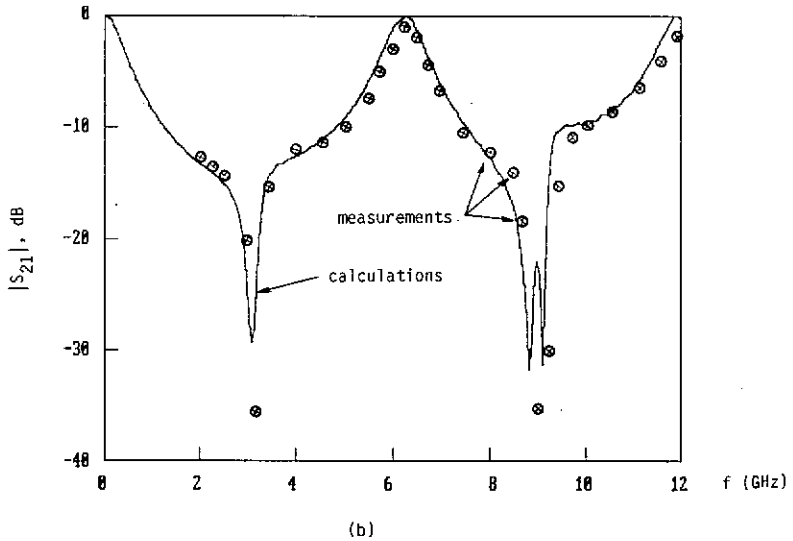

(b)

Fig. 26. Comparison of FD-TD modeling predictions with measurements of $|S_{21}|$ for a two-port microstrip ring circuit: (a) geometry and gridding of microstrip circuit; (b) comparative results over 2–12 GHz [38].

ds within a highly
) MHz; (b) along a

especially at higher frequencies where media dispersion can become important.

9. FD-TD inverse scattering reconstructions in one and two dimensions

Initial work has demonstrated the possibility of accurately reconstructing one-dimensional profiles of permittivity and conductivity [39], and the shape and dielectric compositions of two-dimensional targets [40, 41] from minimal scattered field pulse response data. The general approach involves setting up a numerical feedback loop which uses a one- or two-dimensional FD-TD code as a forward-scattering element, and a specially constructed non-linear optimization code as the feedback element. FD-TD generates a test pulse response for a trial layering or target shape/composition. The test pulse is compared to the measured pulse, and an error signal is developed. Working on this error signal, the nonlinear optimization element perturbs the trial layering or target shape/composition in a manner to drive down the error. Upon repeated iterations, the proposed layering or target ideally converges to the actual one, a strategy similar to that of [42].

The advantage of working in the time domain is that a layered medium or target shape can be reconstructed sequentially in time as the wavefront of the incident pulse sweeps through, taking advantage of causality. This reduces the complexity of reconstruction since only a portion of the layering or target shape is being generated at each iteration. Advanced strategies for reconstruction in the presence of additive noise may involve the use of prediction/correction, where the trial layer or target shape is considered to be a predictor of the actual case, which is subsequently corrected by optimization of the entire layered medium or target shape using the complete scattered pulse waveform.

Figure 27 shows the application of the basic FD-TD feedback strategy to a one-dimensional layered medium in the absence of noise. Both the electrical permittivity and conductivity of the medium vary in a "sawtooth" manner with depth. The curves show simulated measured data for the reflected pulse for three cases defined by the peak values of the conductivity (0.001 S/m, 0.01 S/m, and 0.1 S/m) and the corresponding spatially coincident peak values of relative permittivity (3, 2, and 4) of the medium. In each case, the incident pulse is assumed to be half-sinusoid spanning 50 cm between zero crossings. Noting that the dark dots superimposed on the "sawtooth" represent the reconstructed values of permittivity and conductivity, we see that the basic FD-TD feedback strategy is quite successful in the absence of noise [39].

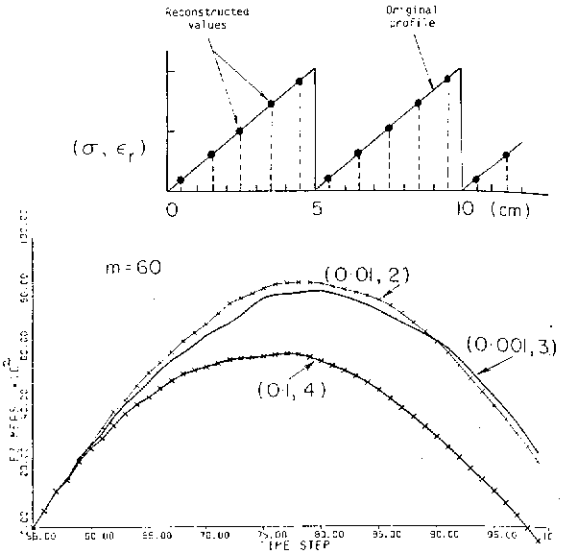

Fig. 27. Application of the FD-TD/feedback strategy to reconstruct a one-dimensional "sawtooth" variation of electrical permittivity and conductivity in the absence of noise [39].

Figure 28 shows the application of the FD-TD feedback strategy to reconstruct a two-dimensional lossy dielectric target. The target is a 30 cm × 30 cm square cylinder having a uniform conductivity of 0.01 S/m, and a tent-like relative permittivity profile which starts at 2.0 at the front and left sides and increases linearly to a peak value of 4.0 at the back corner on the right side. These profiles are

Fig. 28. Applic

illustrated ir
Fig. 28. The
by a TM p
toward the f
top of Fig. 2
sinusoidal t
frequency. F
utilized is th
tered electric
points are lo
and are posit
center line. T
computed sc
nated with a

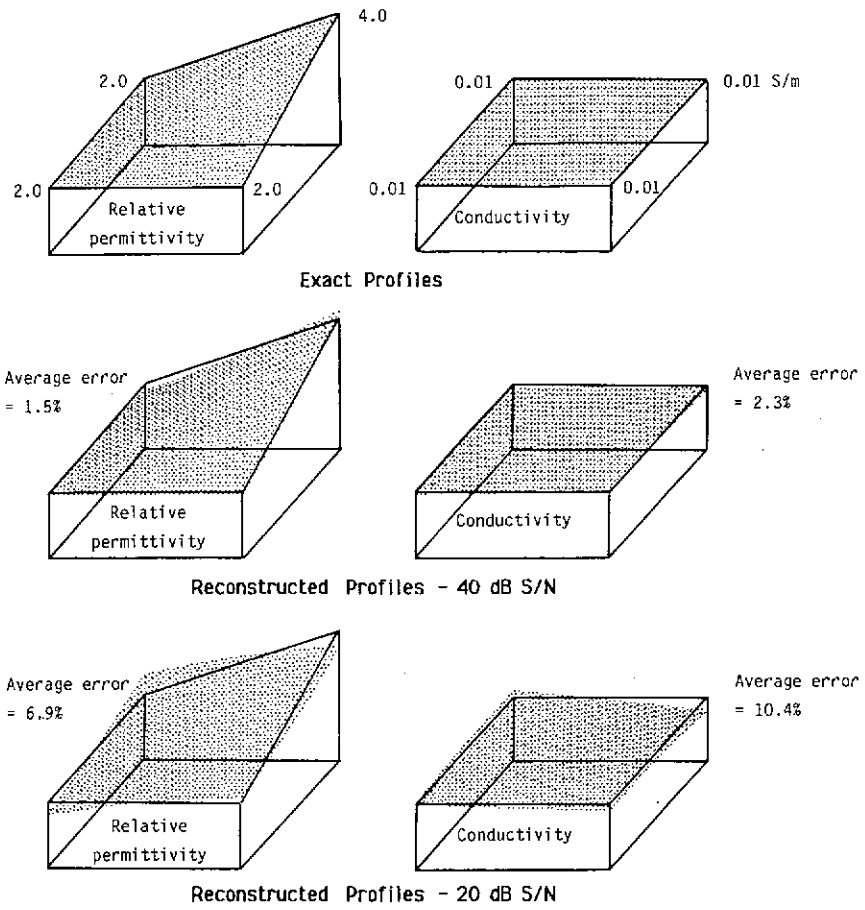

Fig. 28. Application of the FD-TD/feedback strategy to reconstruct a two-dimensional lossy dielectric target in the presence of noise [41].

illustrated in a perspective manner at the top of Fig. 28. The target is assumed to be illuminated by a TM polarized plane wave that is directed toward the front of the target (as visualized at the top of Fig. 28). The incident waveform is a 3-cycle sinusoidal tone burst having a 60 MHz carrier frequency. For the reconstruction, the only data utilized is the time-domain waveform of the scattered electric field as observed at two points. These points are located 1 m from the front of the target, and are positioned 15 cm to either side of the target center line. To simulate measured data, the FD-TD computed scattered field waveforms are contaminated with additive Gaussian noise. In all of the reconstructions, the target shape and location is assumed to be known.

From Fig. 28, we see that for a signal/noise ratio of 40 dB, the average error in the reconstructed permittivity and conductivity profiles is 1.5% and 2.3% respectively. If the signal/noise ratio is reduced to 20 dB, the average errors increase to 6.9% and 10.4%, respectively [41]. Research is ongoing to determine means of improving the noise performance, especially using predictor/corrector techniques briefly discussed earlier. Given the relatively small amount of scattered field data utilized, the FD-TD feedback strategy appears promising for future development.

10. Very large-scale computer software

The FD-TD method is naturally suited for large-scale processing by state-of-the-art vector supercomputers and concurrent processors. This is because essentially all of the arithmetic operations involved in a typical FD-TD run can be vectorized or cast into a highly concurrent format. Further, the $O(N)$ demand for computer memory and clock cycles (where N is the number of lattice space cells) is dimensionally low, and permits three-dimensional FD-TD models of structures spanning 50–100 λ_0 to be anticipated by the early 1990s.

Table 1
Computation times

Machine	10-wavelength model present FD-TD code*
VAX 11/780 (no floating-point accelerator)	40.0 h
Cray-2 (single processor, using the VAX Fortran)	12.0 min
Cray-2 (single processor, some code optimization)	3.0 min
Cray-2 (four processors, some code optimization)	1 min (est.)
True 10 Gflop machine	2 sec (est.)

* $1.55 \cdot 10^6$ unknown field vector components, 661 time steps (T-shaped target). The complete bistatic RCS pattern is obtained for a single illumination angle at a single frequency. Times are increased by 50%–100% if an impulsive illumination/Fourier transform is used to obtain the bistatic RCS pattern at a multiplicity of frequencies within the spectrum of the impulsive illumination.

Let us now consider computation times of present FD-TD codes. Table 1 lists computation times (derived either from benchmark runs or based on analysts' estimates) for modeling one illumination angle of a 10 λ_0 three-dimensional structure using the present FD-TD code. Note that the fourth computing system listed in the table is a hypothetical next-generation machine operating at an average rate of 10 Gflops. This capability is generally expected to be available in the early 1990s.

From Table 1, it is fairly clear that steadily advancing supercomputer technology will permit routine engineering usage of FD-TD for modeling electromagnetic wave interactions with electrically-large structures by 1995.

An interesting prospect that has recently arisen is the reduction of the $O(N)$ computational burden of FD-TD to $O(N^{1/3})$. This possibility is a consequence of the appearance of the Connection Machine (CM), which has tens of thousands of simple processors and associated memories arranged in a highly efficient manner for processor-to-processor communication. With the CM, a single processor could be assigned to store and time-step a single row of vector field components in a three-dimensional FD-TD space lattice. For example, $1.5 \cdot 10^6$ processors would be sufficient to store the 6 Cartesian components of E and H for each of the 500×500 rows of a cubic lattice spanning 50 λ_0 (assuming 10 cells/λ_0 resolution). FD-TD time-stepping would be performed via row operations mapped onto the individual CM processors. These row operations would be performed concurrently. Thus, for a fixed number of time steps, the total running time would be proportional to the time needed to perform a single row operation, which in turn would be proportional to the number of field vector components in the row, or $O(N^{1/3})$.

For the 50 λ_0 cubic lattice noted above, this would imply a dimensional reduction of the computational burden from $O(500^3)$ to $O(500)$, a tremendous benefit. As a result, it is conceivable that a suitably scaled CM could model one illumination angle of a 50 λ_0 three-dimensional structure in only a few seconds, achieving effective floating-point rates in the order of 100 Gflops. For this reason, FD-TD software development for the CM is a promising area of research for developing ultralarge numerical models of electromagnetic wave interactions with complex structures.

11. Conclusion

This paper has reviewed the basic formulation of the FD-TD numerical modeling approach for Maxwell's equations. A number of two- and three-

dimensional examples of FD-TD modeling of electromagnetic wave interactions with structures were provided to indicate the accuracy and breadth of FD-TD applications. The objects modeled range in nature from simple geometric shapes to extremely complex aerospace and biological systems. In all cases studied to date where rigorous analytical, code-to-code, or experimental validations were possible, FD-TD predictive data for penetrating and scattered near fields as well as radar cross section were in excellent agreement with benchmark data. It was also shown that opportunities are arising in applying FD-TD to rapidly time-varying systems, microwave circuits, and inverse scattering. With continuing advances in FD-TD modeling theory, as well as continuing advances in vector and concurrent supercomputer technology, there is a strong possibility that FD-TD numerical modeling will occupy an important place in high-frequency engineering electromagnetics as we move into the 1990s.

Acknowledgment

The author wishes to acknowledge the research contributions of his colleagues, Prof. K.R. Umashankar of the University of Illinois at Chicago and Prof. G.A. Kriegsmann of Northwestern University. Contributions of graduate students at these two institutions, especially Mr. Ben Beker, Mr. Jeffrey Blaschak, Mr. Fady Harfoush, Mr. Thomas Jurgens, Mr. Thomas Moore, and Mr. Mark Strickel are also gratefully acknowledged. The author also wishes to acknowledge the support of his sponsors, past and present, including the U.S. Air Force Rome Air Development Center (Contracts F30602-77-C-0163, F30602-79-C-0039, F30602-80-C-0302, and F19628-82-C-0140); Lawrence Livermore National Laboratory (Contract 6599805); NASA Lewis Research Center (Grant NAG 3-635); National Science Foundation (Grants ECS-8515777 and ASC-8811273); and Office of Naval Research Contract N00014-88-K-0475.

References

[1] K.S. Yee, "Numerical solution of initial boundary value problems involving Maxwell's equations in isotropic media", *IEEE Trans. Antennas Propagat. 14*, 302-307 (1966).

[2] A. Taflove and M.E. Brodwin, "Numerical solution of steady-state electromagnetic scattering problems using the time-dependent Maxwell's equations", *IEEE Trans. Microwave Theory Tech. 23*, 623-630 (1975).

[3] G.A. Kriegsmann, "Exploiting the limiting amplitude principle to numerically solve scattering problems", *Wave Motion 4*, 371-380 (1982).

[4] A. Taflove and M.E. Brodwin, "Computation of the electromagnetic fields and induced temperatures within a model of the microwave-irradiated human eye", *IEEE Trans. Microwave Theory Tech. 23*, 888-896 (1975).

[5] A. Taflove, "Application of the finite-difference time-domain method to sinusoidal steady state electromagnetic penetration problems", *IEEE Trans Electromagn. Compat. 22*, 191-202 (1980).

[6] A. Taflove and K.R. Umashankar, "A hybrid moment method/finite-difference time-domain approach to electromagnetic coupling and aperture penetration into complex geometries", *IEEE Trans. Antennas Propagat. 30*, 617-627 (1982).

[7] R. Holland, "Threde: a free-field EMP coupling and scattering code", *IEEE Trans. Nuclear Sci. 24*, 2416-2421 (1977).

[8] K.S. Kunz and K.M. Lee, "A three-dimensional finite-difference solution of the external response of an aircraft to a complex transient EM environment I: The method and its implementation", *IEEE Trans. Electromagn. Compat. 20*, 328-333 (1978).

[9] D.E. Meriwether, R. Fisher and F.W. Smith, "On implementing a numeric Huygen's source scheme in a finite-difference program to illuminate scattering bodies", *IEEE Trans. Nuclear Sci. 27*, 1819-1833 (1980).

[10] A. Taflove and K.R. Umashankar, "Advanced numerical modeling of microwave penetration and coupling for complex structures", Final Report No. UCRL-15960, Contract 6599805, Lawrence Livermore Nat. Lab. (1987).

[11] G. Mur, "Absorbing boundary conditions for the finite-difference approximation of the time-domain electromagnetic field equations", *IEEE Trans. Electromagn. Compat. 23*, 377-382 (1981).

[12] K.R. Umashankar and A. Taflove, "A novel method to analyze electromagnetic scattering of complex objects", *IEEE Trans. Electromagn. Compat. 24*, 397-405 (1982).

[13] A. Taflove and KR. Umashankar, "Radar cross section of general three-dimensional scatterers", *IEEE Trans. Electromagn. Compat. 25*, 433-440 (1983).

[14] A. Taflove, K.R. Umashankar and T.G. Jurgens, "Validation of FD-TD modeling of the radar cross section of three-dimensional structures spanning up to nine wavelengths", *IEEE Trans. Antennas Propagat. 33*, 662-666 (1985).

[15] B. Engquist and A. Majda, "Absorbing boundary conditions for the numerical simulation of waves", *Math. Comput. 31*, 629-651 (1977).

[16] L.N. Trefethen and L. Halpern, "Well-posedness of one-way wave equations and absorbing boundary conditions", Rept. 85-30, Inst. Comput. Appl. Sci. and Eng. (ICASE), NASA Langley Res. Center, Hampton, VA (1985).

[17] J.G. Blaschak and G.A. Kriegsmann, "A comparative study of absorbing boundary conditions", *J. Comput. Physics 77*, 109-139 (1988).

[18] D.T. Borup, D.M. Sullivan and O.P. Gandhi, "Comparison of the FFT conjugate gradient method and the finite-difference time-domain method for the 2-D absorption problem", *IEEE Trans. Microwave Theory Tech. 35*, 383-395 (1987).

[19] B. Beker, K.R. Umashankar and A. Taflove, "Numerical analysis and validation of the combined field surface integral equations for electromagnetic scattering by arbitrary shaped two-dimensional anisotropic objects", *IEEE. Trans. Antennas Propagat.*, submitted.

[20] A. Taflove and K.R. Umashankar, "Analytical models for electromagnetic scattering", Final Report RADC-TR-85-87 on contract F19628-82-C-0140, Electromagn. Sci. Div., Rome Air Dev. Center, Hanscom AFB, MA (1985).

[21] K.R. Umashankar, A. Taflove and B. Beker, "Calculation and experimental validation of induced currents on coupled wires in an arbitrary shaped cavity", *IEEE Trans. Antennas Propagat. 35*, 1248-1257 (1987).

[22] T.G. Jurgens, A. Taflove, K.R. Umashankar and T.G. Moore, "FD-TD conformal modeling of smoothly curved targets", *IEEE Trans. Antennas Propagat.*, submitted.

[23] M. Fusco, "FD-TD algorithm in curvilinear coordinates", *IEEE Trans. Antennas Propagat.*, submitted.

[24] V. Shankar and W. Hall, "A time-domain differential solver for electromagnetic scattering problems", *Proc. IEEE 77* (1989).

[25] J.G. Blaschak, G.A. Kriegsmann and A. Taflove, "A study of wave interactions with flanged waveguides and cavities using the on-surface radiation condition method", *Wave Motion 11* (1989).

[26] F. Harfoush, A. Taflove and G.A. Kriegsmann, "A numerical technique for analyzing electromagnetic wave scattering from moving surfaces in one and two dimensions", *IEEE Trans. Antennas Propagat. 37* (1989).

[27] D. De Zutter, "Reflections from linearly vibrating objects: plane mirror at oblique incidence", *IEEE Trans. Antennas Propagat. 30*, 898-903 (1982).

[28] D.R. Wilton and S. Govind, "Incorporation of edge conditions in moment method solutions", *IEEE Trans. Antennas Propagat. 25*, 845-850 (1977).

[29] J. Gilbert and R. Holland, "Implementation of the thin-slot formalism in the finite-difference EMP code THREDII", *IEEE Trans. Nuclear Sci. 28*, 4269-4274 (1981).

[30] K.S. Yee, "A numerical method of solving Maxwell's equations with a coarse grid bordering a fine grid", SGEMP Note #9, Document D-DV-86-0008, D Division, Lawrence Livermore Nat. Lab. (1986).

[31] A. Taflove, K.R. Umashankar, B. Beker, F. Harfoush and K.S. Yee, "Detailed FD-TD analysis of electromagnetic fields penetrating narrow slots and lapped joints in thick conducting screens", *IEEE Trans. Antennas Propagat. 36*, 247-257 (1988).

[32] R. Holland and L. Simpson, "Finite-difference analysis of EMP coupling to thin struts and wires", *IEEE Trans. Electromagn. Compat. 23*, 88-97 (1981).

[33] A. Taflove and K.R. Umashankar, "Evaluation of time-domain electromagnetic coupling techniques. Vol. I: Theory and numerical results", Final Report RADC-TR-80-251 on contract F30602-79-C-0039, Rome Air. Dev. Center, Griffiss AFB, NY (1980).

[34] D.M. Sullivan, D.T. Borup and O.P. Gandhi, "Use of the finite-difference time-domain method in calculating EM absorption in human tissues", *IEEE Trans. Biomed. Eng. 34*, 148-157 (1987).

[35] D.M. Sullivan, O.P. Gandhi and A. Taflove, "Use of the finite-difference time-domain method in calculating EM absorption in man models", *IEEE Trans. Biomed. Eng. 35*, 179-186 (1988).

[36] X. Zhang, J. Fang, K.K. Mei and Y. Liu, "Calculations of the dispersive characteristics of microstrips by the time-domain finite-difference method", *IEEE Trans. Microwave Theory Tech. 36*, 263-267 (1988).

[37] D.H. Choi and W.J. Hoefer, "The finite-difference time-domain method and its application to eigenvalue problems", *IEEE Trans. Microwave Theory Tech. 34*, 1464-1470 (1986).

[38] W.K. Gwarek, "Analysis of arbitrarily-shaped two-dimensional microwave circuits by the finite-difference time-domain method", *IEEE Trans. Microwave Theory Tech. 36*, 738-744 (1988).

[39] K.R. Umashankar, S.K. Chaudhuri and A. Taflove, "Finite-difference time-domain formulation of an inverse scattering scheme for remote sensing of inhomogeneous lossy layered media", *IEEE Trans. Antennas Propagat.*, submitted.

[40] M.A. Strickel, A. Taflove and K.R. Umashankar, "Accurate reconstruction of two-dimensional conducting and homogeneous dielectric target shapes from a single-point TM scattered field pulse response", *IEEE Trans. Antennas Propagat.* submitted.

[41] M.A. Strickel and A. Taflove, "Reconstruction of one- and two-dimensional inhomogeneous dielectric targets using the FD-TD/feedback method", *IEEE Trans. Antennas Propagat.*, submitted.

[42] C.L. Bennett and G.F. Ross, "Time-domain electromagnetics and its applications", *Proc. IEEE 66*, 299-318 (1978).